Analytical Models of Probe Dynamics Effects on NMR Measurements

Mason Greer[a], David Ariando[b,*], Martin Hürlimann[c], Yi-Qiao Song[d], Soumyajit Mandal[b]

[a] *Case Western Reserve University, 10900 Euclid Ave, Cleveland, OH 44106, USA*
[b] *University of Florida, 1064 Center Drive, Gainesville, FL 32611, USA*
[c] *Schlumberger-Doll Research, Cambridge, MA 02139, USA*
[d] *Massachusetts General Hospital, Charlestown, MA 02129, USA*

Abstract

This paper provides a detailed analysis of three common NMR probe circuits (untuned, tuned, and impedance-matched) and studies their effects on multi-pulse experiments, such as those based on the Carr-Purcell-Meiboom-Gill (CPMG) pulse sequence. The magnitude of probe dynamics effects on broadband refocusing pulses are studied as a function of normalized RF bandwidth. Finally, the probe circuit models are integrated with spin dynamics simulations to design hardware-specific RF excitation and refocusing pulses for optimizing user-specified metrics such as signal-to-noise ratio (SNR) in grossly inhomogeneous fields. Preliminary experimental results on untuned probes are also presented.

Keywords: Spin dynamics, probe circuits, pulse design, optimal control theory, low-field NMR.

1. Introduction

Traditional NMR experimental apparatus utilizes impedance matching of the radio frequency (RF) coil to the transmitter and receiver to ensure i) efficient transmission of RF power for spin manipulation, and ii) significant voltage gain with out-of-band noise rejection during reception. We refer to such probes as being impedance-matched. In addition, low-frequency systems, such as for NMR well-logging [1, 2], often use probes that are tuned, but not impedance-matched. In either case, a typical tuning circuit consists of a tuning capacitor (capacitance C) in parallel with the RF coil (inductance L). This LC circuit acts as an analog band-pass filter with a resonance frequency $\omega_r \approx 1/\sqrt{LC}$ and bandwidth $BW \approx \omega_r/Q$,

*Corresponding author
Email addresses: mkg53@case.edu (Mason Greer), dariando@ufl.edu (David Ariando), mhurlimann@gmail.com (Martin Hürlimann), ysong5@mgh.harvard.edu (Yi-Qiao Song), soumyajit@ece.ufl.edu (Soumyajit Mandal)

where R_c and $Q \approx \omega_r L/R_c$ are the series resistance and quality factor of the coil, respectively. The value of Q for typical coil geometries is usually > 50, which ensures that $BW \ll \omega_r$. The dynamics of such a narrow-band circuit begins to affect the measurement when the probe bandwidth becomes comparable to the NMR signal bandwidth, which is approximately $2\omega_1$ for extended samples in a static field gradient. Here $\omega_1 = \gamma B_1 = \pi/(2T_{90})$ is the nutation frequency, where B_1 is the amplitude of the RF magnetic field seen by the spins, and T_{90} is the length of a $\pi/2$ RF pulse.

In the time domain, limited probe bandwidth limits the speed at which transmit pulses can be turned on and off. This effect becomes worse at lower frequencies or high Q coils, which can be illustrated by looking at the rise or fall time of resonant circuits. For example, the voltage envelope across a parallel RLC circuit driven on-resonance rises and falls as $V(t) = V_0\left(1 - e^{-\omega_r t/(2Q)}\right)$ and $V(t) = V_0 e^{-\omega_r t/(2Q)}$, respectively, where V_0 is the steady-state amplitude. Thus, the setting time $\sim 4Q/\omega_r$ increases as ω_r decreases or Q increases, which eventually limits the modulation rate of phase- and amplitude-modulated pulses. In receive mode, the probe band-pass filters the NMR signal. While such filtering removes out of band noise, it also results in distorted and time-delayed waveforms at the receiver output. As for transmit pulses, these effects becomes worse for low-frequency and or high-Q systems. Thus, the severity of probe dynamics effects is inversely proportional to the resonance frequency of the experiment and proportional to coil Q. Many commercial MR tools operate at high frequencies where probe dynamics effects can be ignored. However, these effects can be significant for low-field or high-Q systems, particularly for phase- and frequency-modulated pulses. Such finite bandwidth effects are also relevant for quantum computing experiments which utilize extremely high Q, superconducting detectors [3, 4].

Although most NMR hardware utilizes resonant circuits for transmission and reception, recent advancements have led to non-resonant or untuned probe circuits [5–9]. The transmitters and receivers of such systems directly access the coil directly without the use of tuning and/or matching capacitors, thus greatly increasing the probe bandwidth. However, the absence of impedance matching reduces the power available at the coil, while the absence of voltage gain from a tuned circuit degrades receiver noise figure (NF) and signal-to-noise ratio (SNR). In addition, the lack of tuning and matching does not completely eliminate probe dynamics effects.

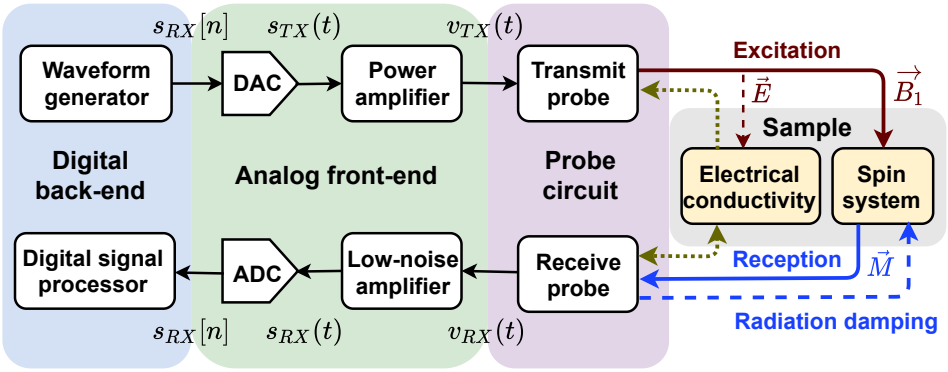

Figure 1: Block diagram of a typical NMR hardware platform. Separate transmit and receive probes are shown for clarity, but are often combined in practice. Here $\vec{E}$ denotes the electric field induced within the sample, which generates eddy currents. ADC = analog-to-digital converter; DAC = digital-to-analog converter.

The fundamental issue is that the transmitter does not directly control the B_1 field seen by the spins, but rather the voltage fed into the probe circuit (whether matched, tuned, or untuned). Similarly, the receiver does not directly sense the precessing magnetization $\vec{M}$, but rather the voltage it induces in the receive coil after it is filtered by the probe. Thus, the probe modifies both the transmit pulses (which alters the spin dynamics) and also the received NMR signals, as shown in Fig. 1. The corresponding transfer functions (TFs) are also sample-dependent due to the bidirectional coupling between the probe and sample, which generates eddy currents (due to electrical conductivity of the sample) [10] and radiation damping effects [11]. The situation is analogous to that for gradient coils in imaging: the gradient amplifier controls either the voltage or current of the gradient coil, not the gradient vector $\vec{G}$.

While a large body of work has focused on modeling the effects of the gradient TF and then removing them using pre-emphasis (i.e., TF inversion) [12, 13], much less work has been carried out on analogous methods for the RF transfer function [14, 15]. The qualitative effects of finite probe bandwidth on RF pulses (known as phase transients or glitches) have long been recognized, particularly in solid-state NMR [16], and pulse sequences that compensate and/or benefit from such "RF imperfections" have also been developed [17]. However, earlier work on quantitatively modeling the effects of tuned and resonant circuits on RF pulses [18, 19] has not directly connected such models to the spin dynamics. In fact, while most NMR hardware on the market utilizes resonant probe circuits, spin dynamics simulators generally do not take the probe dynamics into consideration [20]. This is unfortunate, since NMR spin

dynamics simulations play a crucial role in our understanding of NMR physics and help the development of novel NMR/MRI technologies [20–22]. For example, such simulations have furthered our knowledge of NMR in grossly inhomogeneous B_0 fields [23, 24], aided the development of broadband composite NMR pulses [25–29], enabled modeling of solid-state NMR spectra [30, 31], facilitated studies of large molecules [32], and formed the basis of new MRI techniques [33, 34]. This paper aims to fill the gap between circuit models and spin dynamics by providing a comprehensive summary of probe dynamics and their effects on NMR experiments. Our results are likely to be of particular interest for low-field NMR (where probe dynamics effects are often significant), but they may also be useful for other applications.

Since non-resonant, tuned, and matched probes are all used for NMR measurements, the paper provides a detailed analysis of each circuit. The results are used to study the effects of probe dynamics on pulse transmission and signal reception in various scenarios, including i) single pulses, ii) multi-pulse Carr-Purcell-Meiboom-Gill (CPMG) sequences in grossly-inhomogeneous fields, iii) broadband refocusing pulses for CPMG sequences, and iv) axis-matched excitation and refocusing pulses designed using optimal control theory (OCT). For simplicity, we do not include radiation damping effects, but these can be included in the circuit models by adding a secondary resonator (modeling the spin system) that is inductively-coupled to the RF coil [11, 35]. Also, while our results can be extended to more complicated probe designs by interfacing spin dynamics code to a circuit simulation program such as SPICE [36], we believe that our analytical treatment of several common designs provides useful insights[1].

The paper is organized as follows. Sections 2, 3, and 4 analyze untuned, tuned, and matched probes, respectively. Section 5 discusses the noise analysis and signal detection procedure for all three probe circuits. Various simulation results are described in Section 6, while experimental results are presented in Section 7. Finally, Section 8 concludes the paper.

[1]All the simulation code used in the paper is available from the following public repository: `https://github.com/supertjhok/MATLABSpinDynamics.git`.

2. Untuned Probes

We start by analyzing the transmitter and receiver dynamics for an untuned probe. In its simplest form, an untuned NMR probe simply consists of a coil, which can be modeled as an inductor L in series with a resistor R_c. Some parasitic capacitance C_{par} is always present in parallel with the coil, but we assume the resultant self-resonant frequency $\omega_{SRF} = 1/\sqrt{LC_{par}}$ is much larger than the Larmor frequency ω_0. In this case, C_{par} has negligible effects on the transmitter and receiver dynamics.

2.1. Transmitter Dynamics

The transmitted B_1 drives nonlinear spin dynamics, so the probe dynamics during transmission must be modeled in the time domain. The main goal is to find the coil current I_c (which is proportional to B_1) in terms of the open-circuit transmitter voltage V_s. We use "switched linear" models, which are common in power electronics, to study untuned probes during transmission. The probe is modeled using N linear networks. At certain instants, a controller switches the system from one network to another. The switching action is assumed to i) be much faster than the circuit dynamics, and ii) conserve energy. Thus, it does not affect any state variables (capacitor voltages or inductor currents) in the circuit.

We only need two networks to create a first-order model of an untuned transmitter, as shown in Fig. 2. The first network (Fig. 2(a)) models the transmitter "on" state using a sinusoidal voltage source V_s in series with a resistor $R_{s,on}$. Note that low-frequency NMR transmitters often use a square wave input source. However, only the fundamental component affects the spin dynamics. Thus, a Fourier expansion can be used to replace the square wave by a sinusoid with $4/\pi = 1.27...$ times the amplitude. The second network uses a resistor $R_{s,off}$ to ground to model the transmitter "off" state (Fig. 2(b)). The value of $R_{s,off}$ can be set to a low value just after an RF pulse to model a "Q-switch".

The relevant circuit equations are identical for both networks if we use the appropriate value of R_s and recognize that $V_s = 0$ when the transmitter is off. Defining V_c as the voltage across the coil and using Kirchoff's current law, we have:

$$V_c = L\frac{dI_c}{dt} + R_c I_c \quad \text{and} \quad I_c = \frac{V_s(t) - V_c}{R_s}. \tag{1}$$

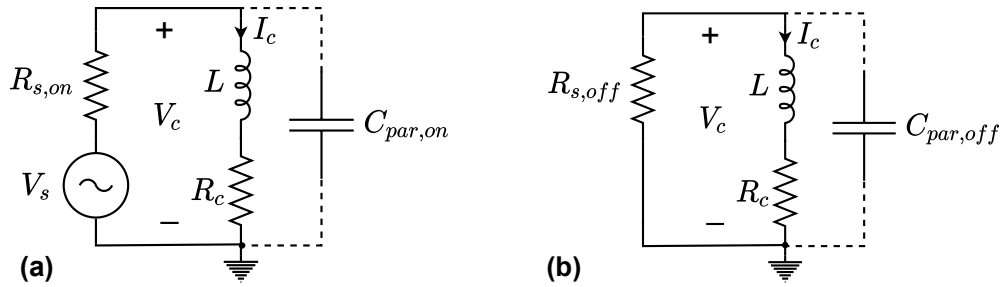

Figure 2: A first-order, two-state model of an untuned NMR probe and transmitter with the transmitter (a) "on", and (b) "off". Here C_{par} is the parallel self-capacitance of the coil.

These equations can be combined into a first-order ordinary differential equation (ODE) given by

$$\frac{dy}{dt} + \frac{y}{\tau_p} = f(t), \tag{2}$$

where $y \equiv I_c$, the probe time constant $\tau_p \equiv L/\left(R_c + R_s\right)$, and the input function $f(t) \equiv V_s(t)/L$. While the first-order dynamics modeled by eqn. (2) can be eliminated by replacing V_s with a RF current source, in practice such wideband current sources are difficult to realize.

We first find a general solution of the associated homogeneous equation by setting $f(t) \to 0$. Physically, this models the natural (not driven) dynamics of the system. The homogeneous equation has the general solution $y_h(t) = y(0)e^{-t/\tau_p}$. Here the time constant τ_p is a measure of how rapidly initial conditions within the coil decay with time.

Next, we find a particular solution of the inhomogeneous (driven) ODE for a complex exponential RF input $f(t) = u(t)e^{i(\omega t+\phi)}$, where ω is the RF frequency and $u(t)$ is the unit step function. The latter models the fact that the input turns on at $t = 0$. A particular analytical solution to this problem is

$$y_d(t) = u(t)Ae^{i(\phi+\theta)}\left[e^{i\omega t} - e^{-t/\tau_p}\right]. \tag{3}$$

Here the steady-state TF is $A\left(\omega\right)e^{i\theta(\omega)} \equiv \tau_p/\left(1 + i\omega\tau_p\right)$ and has the form of a first-order low-pass filter. Also $\omega\tau_p = \omega L/\left(R_c + R_s\right)$, which is the effective quality factor of the probe during transmission, is usually $\gg 1$ at the Larmor frequency. Thus, the steady-state phase-shift is $\theta(\omega) \approx -\pi/2$.

The general solution to the driven ODE is the sum of the homogeneous and particular solutions:

$$y(t) = y_h(t) + y_d(t) = \underbrace{u(t)Ae^{i(\omega t+\phi+\theta)}}_{\text{Steady state}} + \underbrace{\left(y(0) - u(t)Ae^{i(\phi+\theta)}\right)e^{-t/\tau_p}}_{\text{Transient}}, \tag{4}$$

where we have decomposed the solution into its asymptotic (steady-state) and transient components.

2.2. Receiver Dynamics

Assume that the probe and receiver have recovered from the effects of an RF pulse. The probe then acts as a linear time-invariant (LTI) filter with a TF $G_R(\omega) \equiv S_{rx}(\omega)/S_c(\omega)$. Here $S_c(\omega)$ and $S_{rx}(\omega)$ are the signal spectra induced on the coil and across the receiver input terminals, respectively.

Since the NMR signal is detected using Faraday induction, the detected voltage is $V_c(t) = d\varphi/dt$ where φ is the magnetic flux generated by precessing spins within the receive coil. In the frequency domain, this relationship becomes $S_c(\omega) = i\omega(B_1/I)M(\omega)$ where B_1/I is the coil sensitivity function in receive mode [37] and $M(\omega)$ is the magnetization of the sample (as predicted by spin dynamics simulations). Thus, the modified receiver TF becomes

$$\frac{S_{rx}(\omega)}{M(\omega)} = i\omega\left(\frac{B_1}{I}\right)G_R(\omega). \tag{5}$$

Eqn. (5) is valid for all probe designs. In the case of an untuned probe, $G_R(\omega) \approx 1$, i.e., is constant over the bandwidth of interest. Thus the received signal is identical to that induced on the RF coil.

2.3. Generation of OCT Pulses

2.3.1. Eliminating switching transients

A variety of phase-modulated RF pulses can be designed using OCT to fulfill user-defined performance goals, such as maximizing the fidelity of a state-to-state transfer or increasing SNR for a given peak RF power level [25, 26]. For this purpose, the pulse is discretized into a set of segments, each with uniform phase ϕ_n. We would like to remove the transient components produced by the untuned probe during the resultant phase jumps $\phi_n \rightarrow \phi_{n+1}$. Let us assume that the output has reached its steady-state value before the input phase changes from ϕ to ϕ' at time $t = T$. We can simply change

the effective RF phase to $\phi_{eff} = \omega T + \phi$ to use the solution derived earlier (for a step at $t = 0$) in this situation (for a step at $t = T$). The initial amplitude of the transient component is then given by

$$\left(y(T) - Ae^{i(\omega T+\phi'+\theta)}\right) = A\left(e^{i(\omega T+\phi+\theta)} - e^{i(\omega T+\phi'+\theta)}\right) = Ae^{i(\omega T+\theta)}\left(e^{i\phi} - e^{i\phi'}\right).$$

Unfortunately, this quantity is non-zero except for the trivial case of no phase change ($\phi = \phi'$). Therefore the transient component cannot be removed.

However, the situation changes if the input voltage is a sinusoid, as when a single transmit coil is used. In this case $f(t) = u(t)\cos(\omega t + \phi)$, i.e., the real part of the complex exponential RF input. Since the system is linear, the resulting particular solution $y_d(t)$ is simply the real part of the complex solution in eqn. (3). The general solution is thus given by

$$y(t) = \underbrace{u(t)A\cos(\omega t + \phi + \theta)}_{\text{Steady state}} + \underbrace{[y(0) - u(t)A\cos(\phi + \theta)]\, e^{-t/\tau_p}}_{\text{Transient}}. \tag{6}$$

The initial amplitude of the transient component for a phase change at time $t = T$ is given by

$$[y(T) - A\cos(\omega T + \phi' + \theta)] = A[\cos(\omega T + \phi + \theta) - \cos(\omega T + \phi' + \theta)].$$

The condition for cancelling the transient is then given by $\cos(\omega T + \phi + \theta) = \cos(\omega T + \phi' + \theta)$. This equation is satisfied when the steady-state RF waveforms of the previous and current pulse segments intersect. In addition to the trivial solution of no phase change ($\phi = \phi'$), the symmetry of the cosine function about 0 (i.e., $\cos(x) = \cos(-x)$) provides another solution:

$$(\omega T + \phi + \theta) = -(\omega T + \phi' + \theta) \quad \Rightarrow \quad \omega T = -\frac{(\phi + \phi')}{2} - \theta. \tag{7}$$

The intersection points occur twice per RF cycle and are separated by half a cycle, i.e., by a time ΔT such that $\omega(\Delta T) = \pm\pi$. Since $\cos(x \pm \pi) = -\cos(x)$, the values of coil current at these points are also inverses of each other. Thus, the transient components can be canceled by keeping track of the

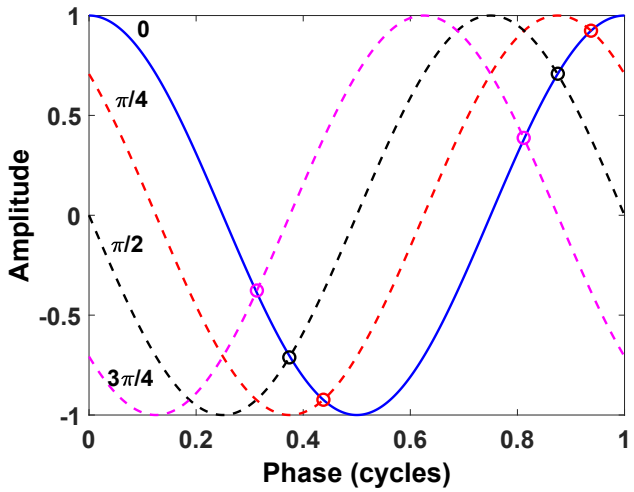

Figure 3: Graphical explanation of the transient elimination principle. The RF waveform corresponding to the initial phase (assumed to be $\phi = 0$) is shown as the solid line, while waveforms corresponding to various phase offsets are shown as dashed lines. It is possible to switch to one of these phases without generating a transient at the times indicated by circles, i.e., when the initial and final waveforms intersect.

absolute RF phase ωT when the phase is switched, as indicated in Fig. 3.

Since intersection points are separated by half an RF cycle, the maximum timing adjustment ΔT_{adj} required for phase-switching to occur at these points is one quarter of a cycle. Thus, $\omega \left| \Delta T_{adj} \right| \leq \pi/2$ suffices to avoid transients. The values of ΔT_{adj} can be found by rewriting the intersection condition as

$$\mathrm{mod}\left(\omega T, \pi\right) = \mathrm{mod}\left[-\frac{\left(\phi + \phi'\right)}{2} - \theta, \pi \right] \equiv \alpha. \tag{8}$$

Writing the absolute RF phase as $\omega T = \pi M + \omega \left(\Delta T_{adj} \right)$ where M is an integer, we find that

$$\omega \left(\Delta T_{adj} \right) = \begin{cases} \alpha, & \alpha \leq \pi/2, \\ -\left(\pi - \alpha \right), & \alpha > \pi/2. \end{cases} \tag{9}$$

Special conditions are required for the first and last pulse segments, as described below:

- First segment: Here the initial condition is $y(0) = 0$, so the design goal is $\cos\left(\omega T + \phi' + \theta\right) = 0$

where ϕ' is the phase of the segment and T is its start time. This condition may be written as

$$\mathrm{mod}\left(\omega T + \phi' + \theta, \pi\right) = \frac{\pi}{2} \quad \text{or} \quad \mathrm{mod}\left(\omega T + \phi' + \theta, \pi\right) = \frac{3\pi}{2}.$$

In the common case when $\omega T = \pi M$ and $\theta \approx -\pi/2$, these conditions reduce to $\phi' = \{0, \pi\}$. The input voltage V_s then reaches its maximum (or minimum) value at $t = T$. Since $\theta \approx -\pi/2$, the steady-state coil current is in quadrature with V_s, and thus is zero at $t = T$. Since the total coil current must be zero at this point to remain continuous, its transient component is also zero.

- Last segment: We require this segment to end with zero coil current, such that no transient response is excited afterwards. Thus, we need $y(T') = 0$, where T' is the time at which the last segment ends. Assuming the current has reached steady-state by this point, this condition may be written as $\cos\left(\omega T' + \phi' + \theta\right) = 0$, or alternatively

$$\mathrm{mod}\left(\omega T' + \phi' + \theta, \pi\right) = \frac{\pi}{2} \quad \text{or} \quad \mathrm{mod}\left(\omega T' + \phi' + \theta, \pi\right) = \frac{3\pi}{2}.$$

Spectrometers designed for low-field measurements often constrain the system clock frequency f_{clk} to be a multiple of the RF frequency, since this provides control over the absolute phase of each RF pulse[2]. Such control is important for obtaining accurate relaxation measurements using CPMG-like multi-pulse sequences when the pulse lengths become comparable to the RF period [38]. In this case, the value of f_{clk} constrains the available phase angles and segment lengths to discrete sets of values. Phases are quantized to the set $k\left(2\pi/N_p\right)$ where N_p is an integer, while pulse segment lengths and delays are quantized to $k\left(2\pi/\left(\omega N_t\right)\right)$ where N_t is the number of steps per RF cycle. Thus, $(\phi + \phi')/2$ will be quantized to $2N_p$ uniformly-spaced values. If the steady-state phase shift θ is quantized to this set, the adjustment angle α for transient cancellation becomes quantized to $2N_p$ values. As a result, $2N_p$ time steps per RF cycle are needed for transient cancellation (i.e., $N_t = 2N_p$). For example, we need 32 steps per cycle ($f_{clk} = 32 \times f_{RF}$) to cancel the transients produced by switching between a set of 16 phases.

[2]General-purpose spectrometers typically do not impose this constraint, instead operating at a fixed value of f_{clk}.

The transient cancellation condition simplifies considerably when phase changes between adjacent pulse segments are constrained to be $\pm\pi$. Examples include symmetric phase-alternating (SPA) refocusing pulses and binary-phase (BPP) excitation pulses [27, 29]. In this case $\phi' = \phi \pm \pi$, so the cancellation condition becomes $(\omega T + \phi + \theta) = \pm\frac{\pi}{2}$ and thus $\cos(\omega T + \phi + \theta) = 0$. Thus, transients are cancelled simply by switching phases at zero-crossings of the coil current. The pulse must also begin and end at zero-crossings to prevent initial and final transients, respectively. Thus, all pulse segment lengths and inter-pulse delays should be integer multiples of half the RF period.

The coil current in the rotating frame is $I_{cr}(t) = I_c(t)e^{-i\omega_0 t}$. For sinusoidal inputs at a frequency $\omega \approx \omega_0$, $I_{cr}(t)$ has three main components: i) Centered around DC: a co-rotating steady-state component of amplitude $I_{ss}/2$ that drives the spin dynamics; ii) Centered around $2\omega_0$: a counter-rotating steady-state component of amplitude $I_{ss}/2$ that causes second-order effects such as the Bloch-Siegert shift [39]; and iii) Centered around ω_0: probe transients of amplitude I_{tran}. The second and third terms have negligible effects on the spin dynamics if $\omega_0 \gg \omega_1$ and the coil only generates fields perpendicular to the static field. However, the DC component of the transients (i.e., the third term) will effectively shift the resonance frequency ω_0 when the coil current generates a component along the static field, thus inducing a phase shift in the transverse magnetization. In either case, eliminating the transients reduces transmitter power consumption. The average power dissipated in the coil and transmitter over a duration T is

$$P_{diss} = \frac{(R_c + R_s)}{T}\int_0^T {I_c}^2(t)dt = \frac{(R_c + R_s)}{T}\int_0^T \left[I_{ss}\cos\left(\omega t + \theta + \phi'\right) + I_{tran}e^{-t/\tau_p}\right]^2 dt, \tag{10}$$

where $I_{ss} = A\left(V_s/L\right) = V_s/\left(R\sqrt{\omega^2\tau_p^2 + 1}\right)$ is the steady-state amplitude of the coil current, while $I_{tran} = I_c(0) - I_{ss}\cos(\theta + \phi')$ is the initial amplitude of the transient component. We assume that the integration is performed over many RF cycles, such that $\omega T \gg 1$. The average power dissipation is then

$$\overline{P_{diss}} \approx (R_c + R_s)\left[\frac{I_{ss}^2}{2} + \overline{I_{tran}^2}\left(\frac{1 - e^{-2T/\tau_p}}{2T/\tau_p}\right)\right]. \tag{11}$$

For a phase-modulated pulse, T may be identified as the length of each constant-phase segment, i.e., the inverse of the OCT control bandwidth. If each of these segments is long enough to reach steady-state,

$I_{tran} \approx I_{ss}\left[\cos(\theta+\phi) - \cos(\theta+\phi')\right]$. If in addition the phases (ϕ and ϕ') are uniformly distributed and uncorrelated random variables, the variance of I_{tran} becomes $\overline{I_{tran}^2} = I_{ss}^2$. The fractional increase in power dissipation due to the modulation is then simply $1 + 2\left(1 - e^{-x}\right)/x$, where $x \equiv 2T/\tau_p$. For example, $\overline{P_{diss}}$ increases by 86.5% when $T = \tau_p$ (i.e., $x = 2$). However, this result should be viewed as a worst-case estimate, since in practice the phases of adjacent segments (i.e., ϕ and ϕ') are likely to be correlated, which will reduce the value of $\overline{I_{tran}^2}$.

2.3.2. OCT pulse generation example

Consider an untuned probe with $L = 10$ μH, $R_c = 0.63$ Ω, and a source resistance of $R_s = [2, 20]$ Ω in the transmitter "on" and "off" states, respectively. The transmitter time constant during the pulse is $\tau_p = L/(R_c + R_{s,on}) = 3.8$ μs. The Larmor frequency is assumed to be 0.5 MHz, resulting in a coil Q of 50. Our goal is to generate a phase-modulated, constant-amplitude OCT excitation pulse with 104 segments, each of length $T = 4$ μs (i.e., 2 RF cycles). Since $x = 2T/\tau_p \approx 2.10$, we expect the average transmitter power dissipation to increase by up to 83.5% if transients are not eliminated.

The pulse phases are quantized to one of $N_p = 32$ uniformly-spaced values, corresponding to a clock frequency of $f_{clk} = 32$ MHz. Fig. 4(a) shows the segment lengths required to eliminate the probe transients. These are no longer constant, but vary slightly (by less than half an RF cycle, as expected) depending on the sequence of phases. Figs. 4(b)-(c) show the simulated coil current in the rotating frame before and after transient cancellation, respectively. The former has 47.9% higher power consumption and $\sim$2.2$\times$ higher peak current, in agreement with the analysis. Thus, transient cancellation is beneficial from a power and safety point of view while also eliminating potential effects of the probe transients on the spin dynamics (e.g., time-varying shifts in ω_0).

2.4. Non-Sinusoidal Coil Currents

The solution in eqn. (4) assumes a perfect sine wave across the coil. However, broadband NMR amplifiers often generate distorted waveforms, such as square waves. An analysis of transient cancellation in such situations is included in Appendix A. The analysis shows that the conditions are unaltered when the coil current is symmetric (i.e., contains only odd harmonics), as is often the case in practice.

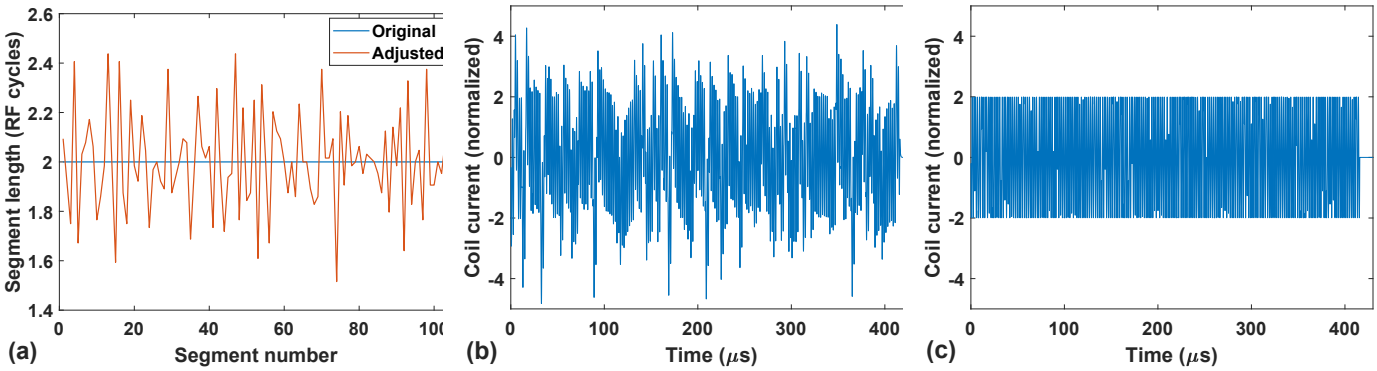

Figure 4: (a) Segment lengths of a phase-modulated, constant-amplitude OCT pulse after the switching instants have been adjusted to eliminate probe settling transients. The original length of each segment was 2 RF cycles. (b)-(c) Simulated coil current in the laboratory frame during the pulse: (b) before, and (c) after transient cancellation. The results have been normalized to a steady-state current magnitude of unity in the rotating frame.

3. Tuned Probes

A tuned NMR probe adds a tuning capacitor C_p in parallel with the coil to form a LC "tank" circuit. The tank circuit acts a narrow-band impedance transformer. It provides voltage gain to the induced NMR signal near its resonant frequency, which lowers the noise figure (NF) of the receiver and thus improves the SNR. The goal of this section is to solve for the current in a RF coil given an input voltage during transmission as well as to derive how a tuned reception affects the received signal.

3.1. Transmitter Dynamics

The dynamics of a tuned probe during transmission can be studied analytically by assuming the same type of two-state "switched linear" model, as shown in Fig. 5. For convenience, we define i) a dimensionless time variable $\tau \equiv \omega_r t$ where $\omega_r = 1/\sqrt{LC}$ is the probe resonance frequency, and ii) the characteristic impedance $Z_0 \equiv \sqrt{L/C}$. Solving for the coil current I_c using circuit analysis (described in Appendix B.1) then results in the second-order ODE

$$\frac{d^2y}{d\tau^2} + 2\gamma\frac{dy}{d\tau} + \omega_n^2 y = f(\tau), \tag{12}$$

which is identical to that of a driven, damped harmonic oscillator. Table 1 summarizes the variables used to define eqn. (12). Physically, ω_n is the natural oscillation frequency of the circuit, γ is the damping coefficient, and $f(\tau)$ is the input (driving function). Note that the damping coefficient increases as

R_s decreases. Many low-frequency NMR transmitters are based on MOSFETs operated as switches. These circuits have an equivalent source resistance R_s, where R_s is approximately equal to the switch on-resistance. Usually R_s is very low (less than a few Ohms), resulting in a large value of γ. In this case the probe is "over-coupled" to the source, which suppresses its internal dynamics. The result is rapid pulse rise and fall times at the expense of lower steady-state current, as shown later.

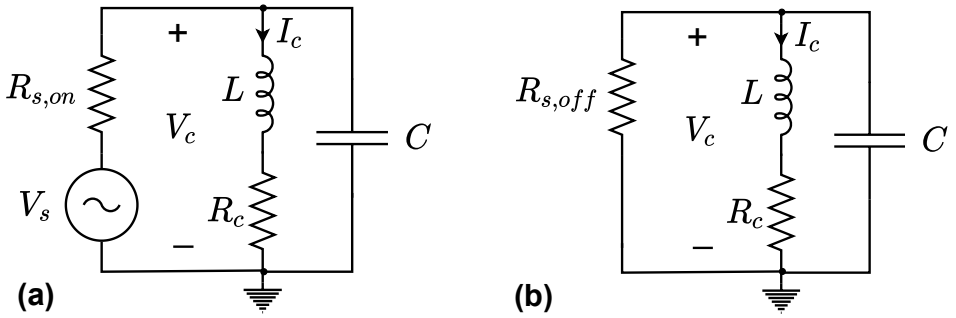

Figure 5: A first-order, two-state model of a tuned NMR probe and transmitter with the transmitter (a) "on", and (b) "off". Here C is the sum of the tuning capacitor and the parallel self-capacitance of the coil.

Eqn. (12) can be analytically solved by decomposing it into homogeneous and particular components. The homogeneous solution is the sum of two exponentials and is given by

$$y_h(\tau) = c_1 e^{\lambda_1 \tau} + c_2 e^{\lambda_2 \tau}, \tag{13}$$

where the variables are defined in Table 1. The values of λ are found by plugging the solution back into the homogeneous ODE and the coefficients c_1 and c_2 are found by using initial conditions, as described in further detail in Appendix B.2.

As described in more detail in Appendix B.3, a particular solution of the inhomogeneous ODE in eqn. (12) was found for a complex exponential input $f(\tau) = u(\tau)e^{i(\omega\tau+\phi)}$, where ω is the normalized (i.e., dimensionless) RF frequency. The result is the sum of asymptotic (steady-state) and transient terms:

$$y_d(\tau) = \frac{u(\tau)e^{i\phi}}{[({\omega_n}^2 - \omega^2) + 2i\gamma\omega]} \left[\underbrace{e^{i\omega\tau}}_{\text{Steady state}} + \underbrace{\frac{(\lambda_2 - i\omega)}{2\alpha} e^{\lambda_1\tau} - \frac{(\lambda_1 - i\omega)}{2\alpha} e^{\lambda_2\tau}}_{\text{Transient}} \right], \tag{14}$$

where the variables are described in Table 1. As in Section 2, the particular solution for a sinusoidal

Table 1: Variable definitions for eqn. (12)

Variable	**Definition**
τ	$t/\sqrt{LC}$
y	I_c
ω_n	$\sqrt{1+\frac{R_c}{R_s}}$
γ	$\frac{1}{2}\left(\frac{R_c}{Z_0}+\frac{Z_0}{R_s}\right)$
$f(\tau)$	$\frac{V_s(\tau)}{R_s}$
α	$\sqrt{\gamma^2-\omega_n^2}$
$\lambda_{1,2}$	$-\gamma \pm \alpha$

input $f(\tau) = u(\tau)\cos(\omega\tau+\phi)$ is simply the real part of the solution $y_d(\tau)$ obtained for the corresponding complex exponential input, i.e., eqn. (14) in this case. Finally, the general solution is the sum of the homogeneous and particular solutions, which is given by $y(\tau) = y_h(\tau) + y_d(\tau)$ in the laboratory frame and $y(\tau)e^{-i(\omega_0\tau)}$ in the rotating frame. The resulting expressions are summarized in Appendix B.4.

The fact that the internal dynamics of a tuned probe are suppressed in the over-coupled case suggests that it should be possible to suppress its transients, as for untuned probes. The analysis in Appendix B.5 confirms that this is indeed the case for tuned probes that are strongly over-coupled. In fact, the transient cancellation condition is identical to that derived in Section 2.

3.2. Receiver Dynamics

The effects of a tuned probe on the induced NMR signal, v_{nmr}, are again expressed through an LTI filter $G_R(\omega) \equiv S_{rx}(\omega)/S_c(\omega)$, where $S_c(\omega)$ is the spectrum of the NMR signal and $S_{rx}(\omega)$ is the spectrum seen by the receiver. We model the receiver admittance as a parallel RC circuit, as is common at typical NMR frequencies. A schematic of the system is shown in Fig. 6(a).

For a simple tuned probe, circuit analysis shows that $G_R(\omega) = [1+(i\omega L+R_c)(i\omega C+G_d+Y_{in})]^{-1}$, where $G_d = 1/R_d$ denotes the conductance of any damping resistor across the probe and $Y_{in} = 1/Z_{in}$ is the input admittance of the receiver. Because the receiver is modeled by a parallel RC circuit,

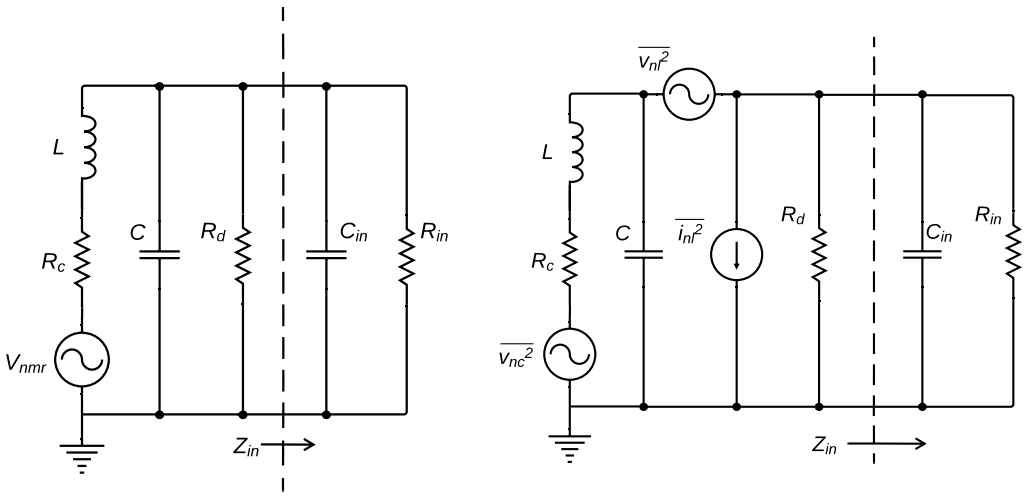

Figure 6: Model of a tuned NMR probe during receive mode for calculating signal (a) and noise (b) transfer functions.

Table 2: Variable definitions for eqn. (15)

Variable	**Definition**
A_0	$\frac{1}{1+R_c(G_d+G_{in})}$
τ_r	$\sqrt{A_0 L\left(C+C_{in}\right)}$
Q_r	$\frac{\tau_r}{L(G_d+G_{in})+R_c(C+C_{in})}$

$Y_{in} = i\omega C_{in} + G_{in}$ and the receiver TF can be written as

$$G_R\left(\omega\right) \equiv \frac{A_0}{\left(i\omega\right)^2 \tau_r^2 + i\omega\left(\tau_r/Q_r\right) + 1} = \frac{A_0}{\left(1-\omega^2\tau_r^2\right) + i\left(\omega\tau_r/Q_r\right)}, \tag{15}$$

where the variables are defined in Table 2. The TF is that of a second-order resonant low-pass filter where A_0 is the DC gain, τ_r is the natural time constant, and Q_r is the probe quality factor in receive mode. The resonant frequency and 3 dB bandwidth of the filter are $1/\tau_r$ and $1/(Q_r\tau_r)$, respectively. If $Q_r \gg 1$, this frequency also results in the largest signal gain, given by $\left|G_R\left(\omega\right)\right|_{\max} = A_0 Q_r$.

For many low-frequency NMR systems, the input impedance of the receiver is much larger than that of the probe, i.e., $C_{in} \ll C$ and $G_{in}R_c \ll 1$. The constants in the receiver TF then simplify to $A_0 \approx \frac{1}{1+R_cG_d} \approx 1$, $\tau_r \approx \sqrt{LC} = 1/\omega_r$ (such that the probe resonant frequencies are identical in transmit and receive mode) and $Q_r \approx \frac{Q}{1+Q(Z_0/R_d)}$ where $Q = Z_0/R_c$ is the quality factor of the coil at ω_r. Thus,

the -3 dB bandwidth of the receive-mode TF becomes $BW \approx \omega_r/Q$, which is much smaller than the transmit-mode bandwidth. This is because the input and source impedances are different; typically $|Z_{in}| \gg R_s$, such that the probe is under-coupled in receive mode but over-coupled in transmit mode.

The phase of the receiver TF is $\theta_r = -\tan^{-1}\left[(\omega\tau_r/Q_r)\,/\,(1-\omega^2\tau_r^2)\right]$, which starts from 0 at DC, reaches $-\pi/2$ at resonance ($\omega\tau_r = 1$), and ends at $-\pi$ at high frequencies. The resulting group delay is

$$\tau_g = \frac{d\theta_r}{d\omega} = \left(\frac{\tau_r}{Q_r}\right)\frac{1+\omega^2\tau_r^2}{\left(1-\omega^2\tau_r^2\right)^2+\left(\omega\tau_r/Q_r\right)^2} = \left(\frac{\tau_r}{Q_r {A_0}^2}\right)|G_R(\omega)|^2\left(1+\omega^2\tau_r^2\right). \tag{16}$$

The group delay is maximized at resonance, where it is equal to $\tau_{g0} = 2Q_r\tau_r$, and decreases to $\tau_{g0}/2$ when the signal gain decreases by 3 dB; the average delay over the 3 dB receiver bandwidth is $\approx 0.75\tau_{g0}$.

Maximum voltage gain for on-resonance NMR signals occurs when the probe is tuned, i.e., when $\omega_0\tau_r = 1$ where ω_0 is the nominal Larmor frequency. In this case the received echoes are time-delayed by $\tau_g = \beta\tau_{g0}$, where $0 < \beta < 1$ depends on their bandwidth relative to the probe; β increases as echo bandwidth decreases, and approaches 1 when the echoes become much more narrowband than the probe. The resulting time delay can be significant for high-Q probes at low Larmor frequencies. Additionally, the frequency-dependent delay introduces an imaginary component to the echo spectrum that is anti-symmetric about ω_0, and therefore not removable by simple phase rotation. Instead, a frequency-dependent phase correction, $\exp\left(i\Delta\omega_0\tau_g(\omega)\right)$, must be applied, where $\tau_g(\omega)$ is the signal delay and $\Delta\omega_0 \equiv \omega - \omega_0$ is the NMR offset frequency. To first order, one can replace $\tau_g(\omega)$ with its average value over the signal bandwidth, which is also equivalent to time-shifting the signal acquisition window.

4. Matched Probes

An impedance-matched NMR probe requires both a parallel tuning capacitor and a series matching capacitor, as depicted in Fig. 7 where C_1 and C_2 are the tuning and matching capacitors respectively. The capacitors C_1 and C_2 ensure impedance matching (and thus maximum power transfer) at the Larmor frequency ω_0. Impedance matching implies that $Z_{in}(\omega_0) = R_s$, where Z_{in} is the input impedance "looking into" the probe. Note that while other capacitive matching circuits are possible, we consider this "shunt tuned, series matched" design since it works well for a wide range of coils. However, neither very small

low-Q coils, nor very large high-Q coils can be impedance-matched using this circuit. In the latter case, a "series-tuned, shunt matched" circuit (i.e., an input-output reversed version) is often used instead.

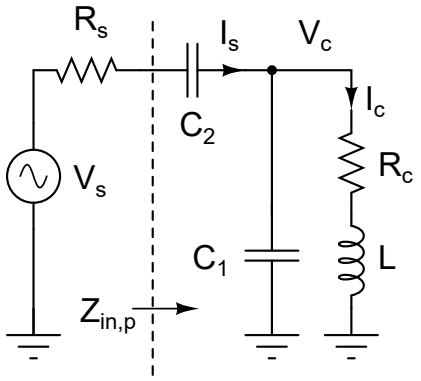

Figure 7: Circuit model of a matched NMR probe during transmission.

4.1. Transmitter Dynamics

A matched transmitter can be modeled as a voltage source V_s in series with a fixed resistance R_s (typically 50 Ω), so a two-state model is not required. The relationship between the open-circuit transmitter voltage V_s and the coil current I_c can thus be derived using the circuit shown in Fig. 7. Here $Z_{in,p}$ is the input impedance of the probe; for a perfectly matched probe, $Z_{in,p} = R_s$.

4.1.1. Solving for the coil current

Given the capacitor values, the coil current can be found in a similar manner as for untuned and tuned probes. In the Laplace domain, the relevant circuit equations are $V_c = (sL+R_c)I_c$, $I_s = sC_1V_c+I_c$, and $V_c = V_s - I_sR_s - \frac{I_s}{sC_2}$, where V_c is the coil voltage and I_s is the current supplied by the source. As described in detail in Appendix C.1, we define a dimensionless time variable $\tau = t/\sqrt{LC_1} \equiv \omega_p t$ and then use an inverse Laplace transform to obtain the third-order ODE

$$\frac{d^3I_c}{d\tau^3} + c_3\frac{d^2I_c}{d\tau^2} + c_2\frac{dI_c}{d\tau} + c_1I_c = \frac{1}{R_s}\frac{dV_s}{d\tau}, \tag{17}$$

where c_1, c_2, and c_3 are constants defined in Table 3. Note that ω_p is not equal to the impedance-matched (i.e., resonant) frequency of the probe, which is again denoted by ω_r; typically $\omega_p > \omega_r$.

Table 3: Variable definitions for eqn. (17)

Variable	**Definition**
ω_p	$\sqrt{LC_1}$
τ	$\omega_p t$
Z_0	$\sqrt{L/C_1}$
m	$\frac{C_1}{C_2}$
c_1	$\frac{mZ_0}{R_s}$
c_2	$c_2 = \left((m+1)\frac{R_c}{R_s} + 1\right)$
c_3	$c_3 = \left((m+1)\frac{Z_0}{R_s} + \frac{R_c}{Z_0}\right)$

Eqn. (17) can be further simplified by normalizing the coil current I_c to its steady-state value for a perfectly-matched probe (denoted by I_{c0}). In Appendix C.1, we use an energy conservation argument to find that $I_{c0} = V_{s0}/\left(2\sqrt{R_c R_s}\right)$, where V_{s0} is the amplitude of V_s. Thus, the normalized ODE becomes

$$\frac{d^3 I_{cn}}{d\tau^3} + c_3 \frac{d^2 I_{cn}}{d\tau^2} + c_2 \frac{dI_{cn}}{d\tau} + c_1 I_{cn} = \frac{2}{V_{s0}} \sqrt{\frac{R_c}{R_s}} \frac{dV_s}{d\tau}. \tag{18}$$

In general, we are interested in complex exponential inputs $V_s(\tau) = V_{s0} e^{i(\omega\tau+\phi)}$ where ω is the normalized RF frequency (i.e., scaled by $1/\omega_p$) and ϕ is the phase of the pulse in the rotating frame. The resulting complex coil current is denoted by $I_{cn}(\tau)$. In some cases (e.g., for very short RF pulses) the absolute phase, ψ, of the input waveform should also be considered [38], such that $V_s(\tau) = V_{s0} e^{i(\omega\tau+\phi+\psi)}$. Finally, the current in the rotating frame can be estimated as $I_{cr}(\tau) = I_{cn}(\tau) e^{-i(\omega_0\tau+\psi)}$.

4.1.2. Effects of discontinuities

In practice the input voltage waveform $V_s(\tau)$ has discontinuities, e.g., at the start and end of each RF pulse. Additional discontinuities can also occur within composite RF pulses due to amplitude and phase modulation. The derivative $dV_s/d\tau$ for the real part of the input waveform at such discontinuities has an additional term proportional to the size of the jump that is given by $\delta(\tau - \tau_i)\left[A_i \sin(\omega\tau + \phi_i + \psi) - A_{i+1} \sin(\omega\tau + \phi_{i+1} + \psi)\right]$, where τ_i is the instant at which the discontinuity occurs, $(A_i,\ \phi_i)$ and $(A_{i+1},\ \phi_{i+1})$ are the pulse amplitudes and phases before and after the

discontinuity, respectively, and $\delta(\tau)$ is the Dirac delta function. A similar term occurs for the imaginary part of the input waveform, but with $\sin(\cdot)$ replaced by $\cos(\cdot)$. The response of the coil current to each perturbation is a scaled version of the impulse response $h(\tau)$ of a linear system with TF given by

$$TF(\sigma) = \frac{I_{cn}(\sigma)}{\sigma V_s(\sigma)} = 2\sqrt{\frac{R_c}{R_s}}\left(\frac{1}{\sigma^3 + c_3\sigma^2 + c_2\sigma + c_1}\right), \tag{19}$$

where $\sigma = s/\omega_p$ is a normalized (i.e., dimensionless) Laplace-domain variable. These impulse responses (which are sinusoidal oscillations with decaying exponential envelopes) should be added to the solution of the ODE before it is converted to the rotating frame. Finally, note that the transients arise from a third-order system and thus depend on the initial values of I_c and its first two derivatives. Since is not possible to ensure that all these quantities remain continuous by simply adjusting the switching instants, in general these transients cannot be removed (unlike for untuned and over-coupled tuned probes).

4.2. Receiver Dynamics

The relationship between the coil voltage V_{in} induced by the precessing nuclear spins and the voltage V_{out} seen by the receiver can be modeled using the circuit shown in Fig. 8(a). We have assumed that the receiver input impedance Z_{in} is equal to the transmitter output impedance R_s, as is often the case.

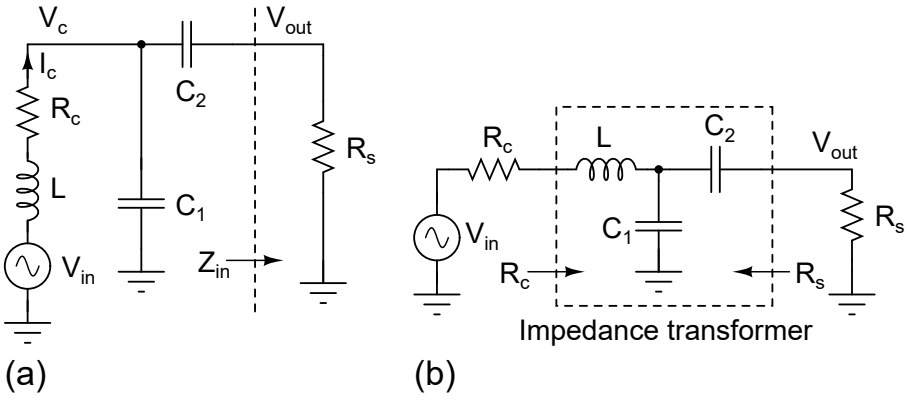

Figure 8: Circuit model of a matched NMR probe during reception: (a) typical view, (b) redrawn to emphasize its function as an impedance transformer.

Circuit analysis (described in detail in Appendix C.2) shows that the resulting TF is

$$G_R(\sigma) = \frac{V_{out}}{V_{in}} = \frac{\sigma}{\sigma^3 + c_3\sigma^2 + c_2\sigma + c_1}, \tag{20}$$

where c_i ($i = \{1, 2, 3\}$) has the same definitions as in the transmitter model.

The frequency-domain receiver TF, $G_R(\omega)$, is found by substituting $\sigma = i\omega/\omega_p$ in eqn. (20). The maximum steady-state voltage gain of the probe (i.e., the peak magnitude of $G_R(\omega)$) can be estimated via an energy conservation argument. For this purpose, consider the redrawn version of the probe circuit shown in Fig. 8(b). Under impedance-matched conditions, the impedance seen looking into the LC network (i.e., the impedance transformer) from its input and output ports must be equal to R_c and R_s, respectively. Thus, a voltage of $V_{in}/2$ appears across the input port, such that the power supplied to the LC network is $P_{in} = (V_{in}/2)^2/(2R_c) = V_{in}^2/(8R_c)$. Assuming the network is lossless, all the power is delivered to the output port, such that $P_{out} = V_{out}^2/(2R_s) = P_{in}$. As a result, $|G_R(\omega)|_{\max} = (V_{out}/V_{in}) = (1/2)\sqrt{R_s/R_c}$. Finally, it can be shown that the -3 dB bandwidth of the receive-mode TF is $BW \approx 2\omega_r/Q$, which is $2\times$ larger than for a tuned probe at the same frequency[3].

It is also interesting to compare the expression for the receiver TF with that in transmit mode. Using our earlier results, we find that

$$\frac{I_c}{V_s/R_s} = \frac{\sigma}{\sigma^3 + c_3\sigma^2 + c_2\sigma + c_1}. \tag{21}$$

Thus, the voltage-mode TF $G_R(\sigma) = V_{out}/V_{in}$ in receive mode is identical to the current-mode TF $I_c/\left(V_s/R_s\right)$ in transmit mode. This is because the LC network (excluding the terminal resistances R_c and R_s) is passive and lossless and thus conserves energy. As a result, $V_{in}I_{in} = V_{out}I_{out}$ and $V_{out}/V_{in} = I_{in}/I_{out}$, i.e., the circuit behaves as an ideal transformer. This explains why we get the same TF when we reverse the input and output ports and replace voltage with current.

5. Noise and Signal Detection

By itself, the linear filtering provided by $G_R(\omega)$ does not preclude accurate measurements since it can be estimated and removed via inverse filtering (i.e., deconvolution). In particular, the received signal, which is denoted by $S_{rx}(\omega) = S_c(\omega)G_R(\omega)$, can be passed through an inverse filter $G_R^{-1}(\omega)$ to recover

[3]The factor of 2 arises from the fact that R_c and R_s dissipate equal amounts of power when the probe is impedance-matched.

$S_c(\omega)$, the induced NMR signal on the coil. In general $G_R^{-1}(\omega)$ will not be causal, but this is acceptable for pre-recorded data. In practice, however, the inversion process is numerically ill-conditioned for noisy inputs. Thus, it is important to analyze how measurement noise is affected by the probe.

5.1. Noise Model

Both the winding resistance R_w of the coil and losses within the sample contribute additive noise to the NMR signal. Both the skin and proximity effects cause winding resistance to increase with frequency approximately as $R_w(\omega) \propto \omega^{1/2}$, although analytical expressions are generally not available [40]. In addition, dielectric and conductive losses within the sample result in effective series resistances that increase with frequency as $R_e(\omega) \propto \omega^3$ and $R_m(\omega) \propto \omega^2$, respectively [10, 37]. However, the bandwidth of interest for NMR is usually no larger than $\pm 5\omega_1$ around the Larmor frequency. Thus, these fundamental noise sources can be assumed to be nearly frequency-independent (i.e., white) over the measurement bandwidth as long as $\omega_0 \gg \omega_1$. Their combined effects are therefore modeled by $R_c(\omega_0) = R_w(\omega_0) + R_e(\omega_0) + R_m(\omega_0)$, the total Larmor frequency-dependent series resistance of the coil. The power spectral density (PSD) of the noise voltage v_{nc}^2 generated by R_c is given by $N_0 = 4kTR_c$.

The noise generated by R_c (known as "probe noise") has the same TF $G_R(\omega)$ to the receiver input as the NMR signal. Thus, $G_R(\omega)$ is given by 1, Eqn. (15), and Eqn. (C.10) for untuned, tuned, and matched probes, respectively. In general $|G_R(\omega)|$ varies with frequency, so the receiver sees colored probe noise with a frequency-dependent PSD $N_0|G_R(\omega)|^2$.

The total noise at the receiver is the sum of probe noise and the receiver's own input-referred noise. The latter is usually modeled by two noise sources: a series voltage source v_{ni} ("receiver voltage noise") and a shunt current source i_{ni} ("receiver current noise"), as shown in Fig. 6(b) for a tuned probe. Assuming that the two sources are uncorrelated for simplicity, the total voltage noise PSD is given by

$$N(\omega) = \underbrace{N_0|G_R(\omega)|^2}_{\text{Colored probe noise}} + \underbrace{\overline{v_{ni}^2(\omega)}}_{\text{Receiver voltage noise}} + \underbrace{\overline{i_{ni}^2(\omega)}|Z_s(\omega)|^2}_{\text{Receiver current noise}} . \tag{22}$$

Here $\overline{v_{ni}^2(\omega)}$ and $\overline{i_{ni}^2(\omega)}$ are the PSDs of the receiver voltage and current noise sources, respectively, and $Z_s(\omega)$ is the effective impedance across the receiver terminals. The latter is defined as $Z_s = Z_p||Z_{in}$,

where Z_p is the impedance seen by looking into the probe and Z_{in} is the input impedance of the receiver.

The noise figure (NF) of the receiver is defined as the ratio of input and output SNR, and should be as close to 1 (0 dB) as possible. In our case it is given by

$$NF(\omega) = \frac{(S_c(\omega)/N_0)}{\left(S_c(\omega)|G_R(\omega)|^2/N(\omega)\right)} = \frac{N(\omega)}{N_0|G_R(\omega)|^2}, \tag{23}$$

where $S_c(\omega)$ is the spectrum of the NMR signal on the coil.

5.2. Signal Detection Model

In reality, signal acquisition only occurs over a finite acquisition time T_{acq}. This fact can be modeled by windowing the time-domain signal $s(t)$, resulting in the acquired signal $s_a(t) \equiv s(t)w(t)$ where $w(t)$ is a rectangular (i.e., boxcar) window function of length T_{acq}. Alternatively, one can convolve the frequency-domain signal with the spectrum of $w(t)$, resulting in the acquired spectrum $S_a(\omega) = S(\omega) * W(\omega)$ where '$*$' denotes convolution and $W(\omega) = \mathcal{F}\{w(t)\}$ is a sinc function (with $\mathcal{F}\{\cdot\}$ denoting the Fourier transform). The main effect of such windowing is to "smooth out" $S_a(\omega)$ by removing fine spectral details (i.e., features on frequency scales smaller than $1/T_{acq}$, the bandwidth of $W(\omega)$).

In practice, the acquired data has finite SNR, as described in the previous section. When the noise is additive, white, and Gaussian, it is well-known from the signal processing literature that the SNR can be maximized by applying a *matched filter* [41]. Let us denote the acquired data as $r_a(t) = s_a(t) + n_a(t)$, where $s_a(t)$ and $n_a(t)$ are the windowed signal and noise components, respectively. The impulse response of the matched filter is a time-reversed version of the noise-free data, i.e., is given by $h_M(t) = s_a^*(-t)$, while its frequency response is $H_M(\omega) = S_a^*(\omega)$. Thus, the signal component after filtering is given by

$$y_M(t) = s_a(t) * h_M(t) = \int_{-\infty}^{\infty} s_a(\tau)s_a^*(\tau - t)d\tau \tag{24}$$

in the time-domain and $Y_M(\omega) = S_a(\omega)H_M(\omega) = |S_a(\omega)|^2$ in the frequency-domain, respectively. Note that in practice the range of integration in eqn. (24) is limited to $[-T_{acq}/2, T_{acq}/2]$, which does not change the result since $s_a(t) = 0$ outside this range. It is easy to show that the SNR of the filtered

time-domain output is maximal at $t = 0$, where the signal component is given by

$$s_M \equiv y_M(0) = \int_{\infty}^{\infty} s_a(\tau) s_a^*(\tau) d\tau = \int_{\infty}^{\infty} |s_a(\tau)|^2 \, d\tau = \int_{-\infty}^{\infty} |S_a(\omega)|^2 d\omega, \tag{25}$$

and the final equality follows from Parseval's theorem. Eqn. (25) shows that s_M, the peak output of the matched filter, is a measure of total signal energy in both the time and frequency domains[4].

The matched filter described above is sub-optimal when the receiver noise PSD $N(\omega)$ predicted by eqn. (22) is noticeably frequency-dependent (i.e., not white). The effects of such "colored" noise become significant when the probe has less bandwidth than the signal, in which case $N(\omega)$ varies significantly across the signal bandwidth. The optimum solution is to add a "whitening" filter $H_W(\omega) \propto 1/\sqrt{N(\omega)}$ before the matched filter $H_M(\omega)$. The whitening filter converts $N(\omega)$ into white noise, after which the signal can be filtered in the usual way by a modified matched filter $H_M{}'(\omega) = S_a^*(\omega) \, |H_W(\omega)|^2$.

6. Simulation Results

In this section, we use the analytical solutions derived in the earlier sections to compare the performance of untuned, tuned, and matched probes in various scenarios. In general, we expect the importance of probe dynamics to increase with normalized B_1 field strength $\omega_{1n} = \omega_1 / (\omega_r / Q)$, where the numerator and denominator are proportional to the NMR and probe bandwidths, respectively. However, scaling with ω_{1n} is only approximate, since the probe dynamics also depend on other circuit parameters (source resistance, receiver input impedance, etc.). Thus, to facilitate a fair comparison, we assume (unless specified otherwise) that both ω_{1n} and the sample coil properties are identical for all three probe types.

[4]It is worth noting that the term "matched filter" carries a slightly different meaning in NMR spectroscopy. In this context, matched filtering (also known as apodization) refers to time-domain multiplication of a free-induction decay (FID) $r_a(t)$ by the expected FID shape $s_a(t)$ (generally, a decaying exponential) to maximize SNR in the frequency domain. However, the peak output of a conventional matched filter is obtained by summing the same time-domain product $r_a(t)s_a(t)$ (see eqn. (25)), so the two concepts are clearly related. In fact, it can be formally shown that apodization is a special case of conventional matched filtering and yields the same maximum SNR [42].

6.1. Rectangular Pulses

To simulate the actual waveform of an RF pulse with a nominal amplitude profile $k[n]$, we vary the input RF amplitude $V_s[n] = V_{s0}a[n]$ in the sequence $a[n] = [0, k[n], 0]$. For example, $a[n] = [0, k, 0]$ for a nominally-rectangular pulse. The coil current is then computed assuming zero initial conditions for the first non-zero segment in $a[n]$ - either using the analytical solution (for untuned and tuned probes), or by numerically solving the ODE (for matched probes). Using zero initial conditions amounts to assuming that the coil current has completely decayed following the previous RF pulse, which is usually a good assumption. The same solution procedure is applied to later segments $a[n]$, but with appropriate initial conditions. The final zero-amplitude segment allows the pulse ring-down to be included.

Consider an example in which a coil with $L = 10$ μH and $Q = 50$ is driven by a rectangular input pulse at $\omega_0 = 2\pi \times 0.5$ MHz. Typical values were chosen for the source resistance, namely $[R_{s,on}, R_{s,off}] = [2, 20]$ Ω (untuned and tuned probes) and $R_s = 50$ Ω (matched probe). The value of $R_{s,off}$ was chosen to minimize the pulse ring-down time. The relationship $C = 1/(\omega_r^2 L)$ was used to choose a tuning capacitor $C = 10.1$ nF for the tuned probe, with $\omega_r = \omega_0$. Finally, least-squares function minimization was used to estimate capacitor values of $C_1 = 9.0$ nF and $C_2 = 2.5$ nF for the matched probe, again with $\omega_r = \omega_0$.

Fig. 9 shows the simulated coil current in the laboratory frame (top row) and rotating frame (bottom row) for all three probes. The input was a nominally-rectangular pulse with normalized amplitude $k = 1$ and duration $t_P = 25$ μs, corresponding to $\omega_1 = 2\pi \times 10$ kHz and $\omega_{1n} = 1$ for a $\pi/2$ pulse. Both the untuned and tuned probes have minimal effect on the pulse profile in the rotating frame. This is because the untuned probe has little dynamics around ω_0, while those of the tuned probe are strongly suppressed by the low source resistance. However, the limited bandwidth of the matched probe results in relatively long rise and fall times for the pulse. Also, in each case, any discontinuities in $dV_s(\tau)/d\tau$ that are present at the beginning and end of the pulse have little effect on the coil current in the rotating frame.

6.2. Receiver Transfer Functions

Next, we consider the receive-mode TFs $G_R(\omega) = S_{rx}/S_c$ for untuned, tuned, and matched probes using the same coil parameters assumed in the earlier section. The untuned and tuned probes use a

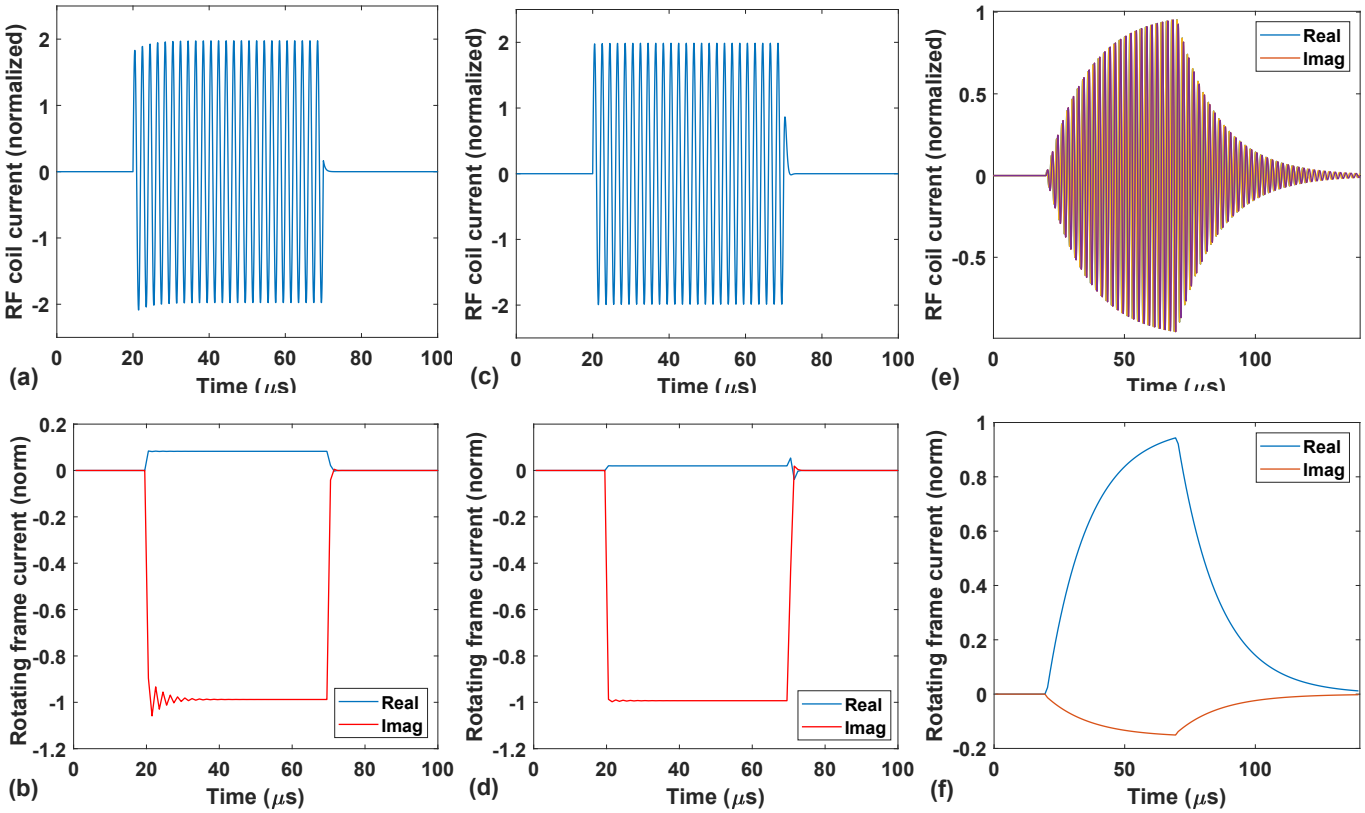

Figure 9: Simulated coil currents generated by (a)-(b) untuned, (c)-(d) tuned, and (e)-(f) matched probes for a nominally-rectangular pulse of length $t_P = 25$ μs at $\omega_r = \omega_0 = 2\pi \times 500$ kHz. (Top row): RF waveforms, (bottom row): rotating frame waveforms. Coil parameters: $L = 10$ μH and $Q = 50$ at ω_r, resulting in $\omega_{1n} = 1$ for a $\pi/2$ pulse. Both untuned and tuned transmitters have a source impedance of $[R_{s,on}, R_{s,off}] = [2, 20]$ Ω, while the matched transmitter has $R_s = 50$ Ω.

high-input-impedance receiver (such that $Q_r \approx Q$, the quality factor of the coil), while the matched probe uses an impedance-matched receiver ($Z_{in} = 50\ \Omega$). The results are shown in Fig. 10 as a function of the frequency offset $\Delta\omega_r = (\omega - \omega_r)$ for $\omega_r = 2\pi \times 500$ kHz. The untuned probe has a nearly constant signal gain of $|G_R(\omega)| \approx 4$; this is set by the turns ratio of a step-up transformer added before the receiver [8]. The tuned probe has a peak gain of $|G_R(\omega)|_{\max} \approx Q$ and -3 dB and -10 dB bandwidths of approximately ω_r/Q and $3\omega_r/Q$, respectively when the coil $Q \gg 1$. Finally, the matched probe has a peak gain of $|G_R(\omega)|_{\max} = (1/2)\sqrt{R_s/R_c} \approx 4.5$ and a -3 dB bandwidth of $\approx 2\omega_r/Q$.

For moderate- and high-Q coils, the voltage gain of the tuned probe exceeds the *peak* gain of the matched probe over a broad frequency range (approximately $\pm 5\omega_1$ in this case, where $\omega_1 = 2\pi \times 10$ kHz). Fundamentally, this is due to the relatively low value of characteristic impedance ($Z_0 = 50\ \Omega$) used by standard RF cables and test equipment. Thus, if we assume similar receiver noise parameters, the NF of the tuned probe will always be better than that of the matched probe, as shown in Fig. 10(b). As a result, receive-mode impedance matching is only beneficial if the distance between probe and receiver, d is large enough for transmission line effects to be significant (roughly, when $d > \lambda/20$, where λ is the electromagnetic wavelength in the cable).

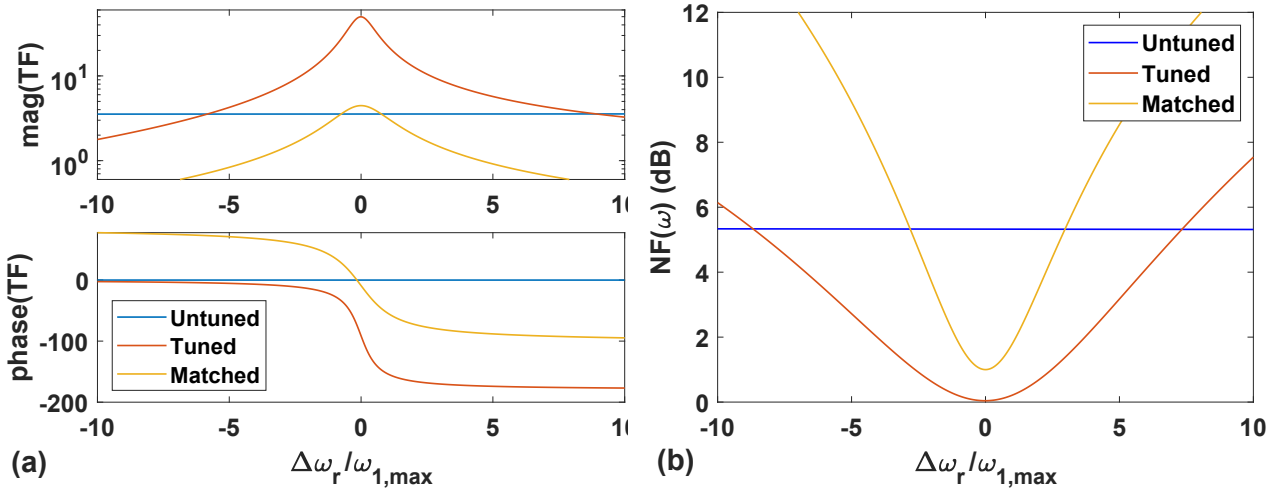

Figure 10: (a) Receive-mode TF, and (b) noise figure (NF) for untuned, tuned, and matched probes at $\omega_r = 2\pi \times 500$ kHz, assuming $\omega_{1,max} = 2\pi \times 10$ kHz (corresponding to $T_{90} = 25\ \mu$s) and the same coil parameters as in the earlier section (resulting in $\omega_{1n} = 1$). The untuned probe uses a $1:4$ step-up transformer to obtain broadband voltage gain before the receiver, as in [8]. Both tuned and untuned probes use a high-input-impedance receiver with $\sqrt{\overline{v_{ni}^2}} = 0.5$ nV/Hz$^{1/2}$ and $\sqrt{\overline{i_{ni}^2}} = 2$ fA/Hz$^{1/2}$. The matched probe uses an impedance-matched receiver with $NF(0) = 1$ dB.

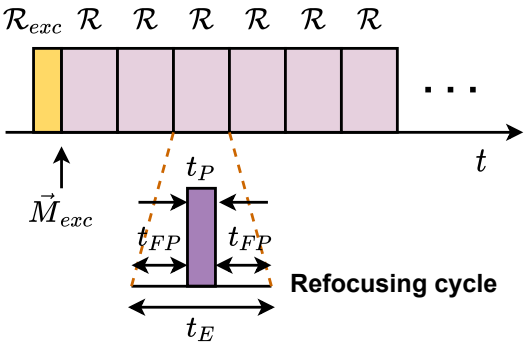

Figure 11: Schematic of CPMG-like pulse sequences, which consist of an initial excitation sequence (denoted by the rotation $\mathcal{R}_{exc}$) and several refocusing cycles of duration t_E (denoted by rotations $\mathcal{R}$). Echoes form at the end of refocusing cycles. Each cycle consists of an RF pulse (duration t_P) and two free precession periods (duration $t_{FP} = (t_E - t_P)/2$).

6.3. CPMG-Like Pulse Sequences

In this section, we discuss the effects of probe dynamics on the CPMG pulse sequence in inhomogeneous B_0 and B_1 fields. For simplicity, we assume that the system is well-modeled by a set of uncoupled spin-1/2 nuclei. We also assume that the echo spacing, t_E, is much shorter than the transverse relaxation time, T_2, and also short enough to make diffusion effects negligible. The propagator from echo to echo for any single member of the ensemble is then accurately approximated by an effective rotation, $\mathcal{R}(\hat{n}, \theta)$, where $\hat{n}$ is the rotation axis, θ is the nutation angle, and both depend on $\Delta\omega_0$ (the local offset of the Larmor frequency from the RF frequency ω), ω_1 (the local strength of the RF field), and t_E [23]. Physically, $\mathcal{R}(\hat{n}, \theta)$ is the overall rotation (in the rotating frame) for a single refocusing cycle, as shown in Fig. 11. Each cycle consists of two periods of free precession and a refocusing pulse; denoting the corresponding rotations by $\mathcal{R}_0$ and $\mathcal{R}_1$, respectively, the overall rotation is $\mathcal{R} = \mathcal{R}_0\mathcal{R}_1\mathcal{R}_0$.

The NMR signal produced by the pulse sequence is modeled using the independent evolution of a large number of isochromats that are distributed over the $(\Delta\omega_0, \omega_1)$ plane. Denoting the underlying distribution as $f(\Delta\omega_0, \omega_1)$ and the initial magnetization due to the excitation pulse as $\vec{M}_{exc}(\Delta\omega_0, \omega_1)$, the magnetization at the nominal center of the k-th echo is then given by

$$S_k(\Delta\omega_0, \omega_1) = f(\Delta\omega_0, \omega_1)\mathcal{R}(\hat{n}, k\theta)\{\vec{M}_{exc}\}e^{-kt_E/T_{2,eff}}, \tag{26}$$

where $\mathcal{R}(\hat{n}, k\theta)\{\vec{M}_{exc}\}$ is the magnetization after k rotations, and $T_{2,eff}$ is the effective time constant

for transverse relaxation.

In a grossly inhomogeneous field, θ varies significantly over $\Delta\omega_0$ and ω_1, and these variations accumulate with echo number k. Thus, after the first few echoes, the detected magnetization is dominated by the component of $\vec{M}_{exc}$ that was aligned with the refocusing axis $\hat{n}$; this is known as the *asymptotic magnetization*. Mathematically, $\mathcal{R}(\hat{n}, k\theta)\{\vec{M}_{exc}\} \approx \left(\hat{n} \cdot \vec{M}_{exc}\right) \hat{n}_\perp$ where $\hat{n}_\perp = n_x + in_y$ is the component of $\hat{n}$ that is transverse to B_0 [23, 28, 29]. Thus, the normalized (i.e., dimensionless) spectrum of the asymptotic echoes detected by the receiver coil is given by

$$S_{asy}(\Delta\omega_0) = (\omega_0 + \Delta\omega_0) \int S_k(\Delta\omega_0, \omega_1)\omega_1 d\omega_1 = (\omega_0 + \Delta\omega_0) \int f(\Delta\omega_0, \omega_1) \left(\hat{n} \cdot \vec{M}_{exc}\right) \hat{n}_\perp \omega_1 d\omega_1, \quad (27)$$

where the factor of $(\omega_0 + \Delta\omega_0) = \omega$ arises from Faraday detection[5], the factor of ω_1 is proportional to the coil sensitivity function B_1/I [37], and we have omitted decay due to relaxation for convenience.

After filtering by the receive-mode TF $G_R(\omega)$, the signal spectrum at the receiver is $S_{rx}(\omega) = G_R(\omega)S_{asy}(\omega)$. Finally, the SNR (in rms units) for asymptotic echoes after matched filtering becomes

$$SNR = \frac{\int_{-\infty}^{\infty} S_a(\omega) H'_M(\omega) d\omega}{\sqrt{\int_{-\infty}^{\infty} N(\omega) \left|H'_M(\omega)\right|^2 d\omega}} = \sqrt{\int_{-\infty}^{\infty} \frac{\left|S_a(\omega)\right|^2}{N(\omega)} d\omega}, \quad (28)$$

where $S_a(\omega) = S_{rx}(\omega) * W(\omega)$ is the received signal after convolution with the acquisition window, and $H_M{}'(\omega) = S_a^*(\omega) \left|H_W(\omega)\right|^2$ is the modified matched filter discussed in Section 5.

6.3.1. Effects of Probe Type

We first simulate the asymptotic magnetization and spin echoes generated by an "ideal" CPMG sequence using rectangular pulses for a linear B_0 gradient field and uniform B_1 amplitude; in this case $f(\Delta\omega_0, \omega_1)$ reduces to a constant. This type of field distribution is a good approximation to that generated by many single-sided magnets, including well-logging tools [2] and low-field imagers [43]. In

[5]The $(\omega_0 + \Delta\omega_0)$ term is nearly constant unless the offset frequency range of interest (approximately $\pm 5\omega_1$) is a significant fraction of the nominal Larmor frequency ω_0. At such low frequencies (and/or high RF power levels), the fact that the initial magnetization (at thermal equilibrium) is proportional to ω should also be included.

this context, "ideal" implies that probe dynamics effects are ignored. These results are then compared to simulations that do include our probe models.

Fig. 12 summarizes the asymptotic CPMG magnetization spectra and time-domain echoes (which are Fourier transform pairs) for a normalized RF bandwidth of $\omega_{1n} = 1$. Here (a) and (b) refer to the ideal system with no probe effects, (c) and (d) refer to an untuned probe, (e) and (f) refer to a tuned probe, and (g) and (h) refer to a matched probe, respectively. Note that the x-axis in Figs. 12(a), (c), (e), and (g) is in units of the normalized offset frequency, i.e., $\Delta\omega_0 = (\omega - \gamma |\mathbf{B}_0|) / \omega_{1,max}$ where ω is the excitation frequency (assumed to be equal to both the average Larmor frequency ω_0 and the probe tuning frequency ω_r) and $\omega_{1,\max}$ is the nominal nutation frequency (assumed to be uniform across the sample). The latter is defined as $\omega_{1,\max} = \gamma B_{1c,\max}$, where $B_{1c,\max}$ is the steady-state magnitude of the circularly polarized component of the RF magnetic field that is orthogonal to B_0.

The simulated spectra (left-hand column of Fig. 12) highlight the main effects of probe circuits on NMR measurements. Firstly, we notice that both the asymptotic magnetization spectrum (S_{asy}) and the received spectrum (S_{rx}) of the untuned probe are very similar to that of the ideal system (Fig. 12(a)), with the exception of a $\approx \pi/2$ phase rotation. This is because the untuned probe is broadband during both transmission and reception, as shown in Figs. 9 and 10, respectively. Secondly, for the tuned probe S_{asy} remains similar to that of the ideal system, while S_{rx} is a band-pass filtered version of it. This is because the tuned probe is broadband during transmission (since the low-impedance transmitter is over-coupled to the probe and suppresses its dynamics) but narrowband during reception. Finally, for the matched probe both S_{rx} and S_{asy} are band-pass filtered because the circuit is narrowband during both transmision and reception. The time-domain echoes (right-hand column of Fig. 12) provide some additional information. Notably, both tuned and matched probes generate asymmetric echo shapes (with fast rise times and slow fall times) due to their causal and band-limited receive-mode TFs $G_R(\omega)$, which result in positive group delay (as analyzed for tuned probes in Section 3). However, the effect is smaller for matched probes due to their larger bandwidth.

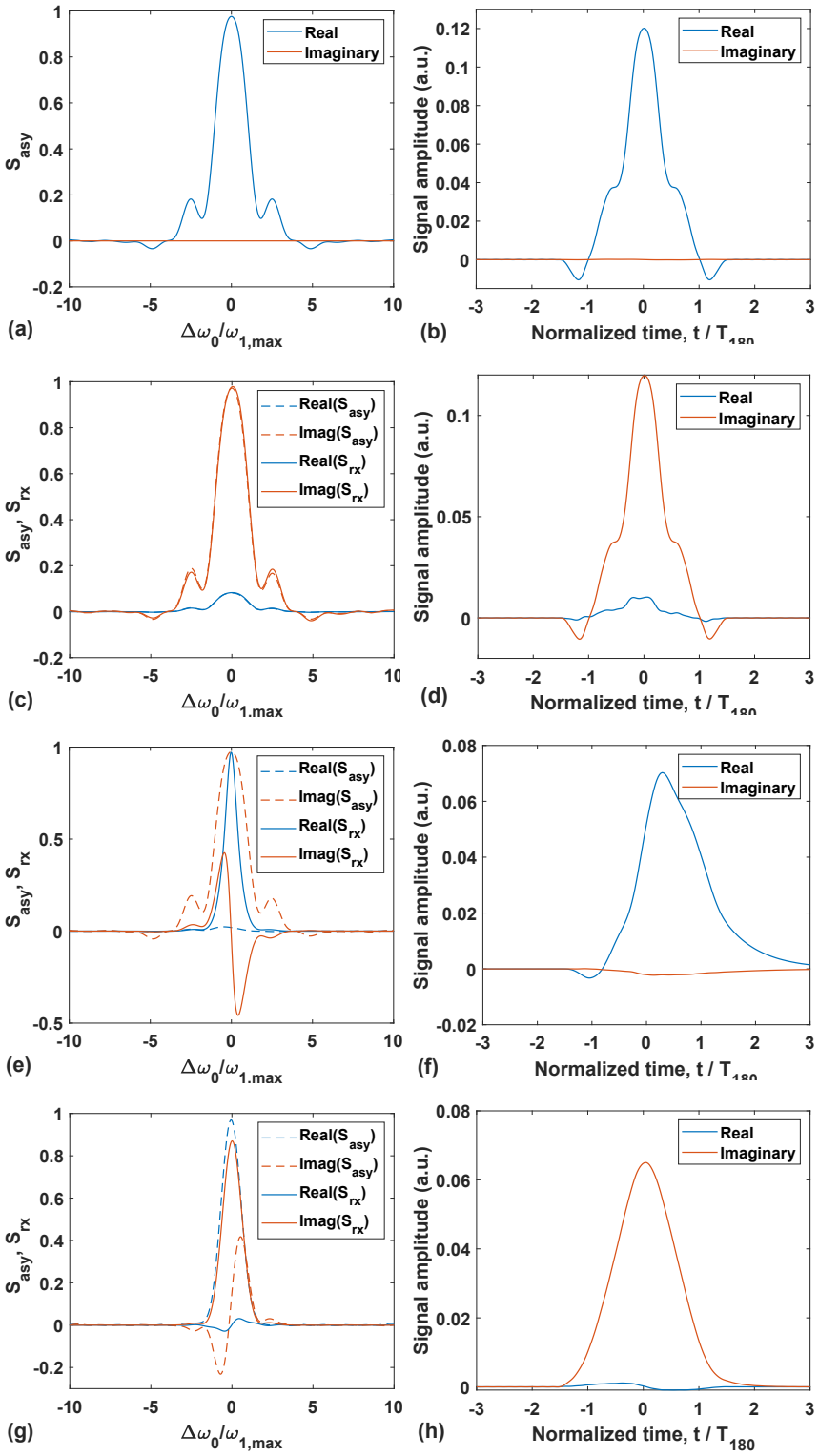

Figure 12: Simulated asymptotic magnetization spectrum (S_{asy}), received spectrum (S_{rx}), and echo shapes for CPMG sequences for a linear B_0 field gradient and uniform B_1, assuming (a)-(b) no probe dynamics, (c)-(d) an untuned probe, (e)-(f) a tuned probe, and (g)-(h) a matched probe. Spectra and echoes are shown in the left and right columns, respectively; S_{rx} has been divided by the peak receive-mode gain for clarity. Other parameters: $\omega_0 = 2\pi\times500$ kHz, $\omega_{1,max} = 2\pi\times10$ kHz (such that $T_{90} = 25$ μs), and the same coil ($L = 10$ μH, $Q = 50$), thus resulting in $\omega_{1n} = 1$ for all the probe designs.

6.3.2. Effects of Probe Bandwidth and Tuning Errors

In this section, we simulate asymptotic echo shapes and SNR of CPMG sequences using nominally-rectangular pulses as a function of coil Q. Other probe and pulse sequence parameters were kept identical to those in the previous section. The results are shown in Figs. 13(a) and (b) for tuned and matched probes, respectively, while Figs. 13(c) summarizes the SNR obtained in both cases. The figure shows that the asymptotic echo shapes become broader in the time-domain as coil Q increases; this is due to reduced probe bandwidth (i.e., increased ω_{1n}). The tuned probe also exhibits increasing group delay $\propto Q$, as expected. However, since the thermal noise PSD generated by the coil decreases $\propto 1/Q$, the SNR (in rms units) continues to increase as $\sqrt{Q}$. It is also worth noting that the tuned probe provides significantly more SNR ($\approx 50\%$ in rms units) over the entire range of Q. This is because of its lower NF over the entire measurement bandwidth, as shown in Fig. 10(b).

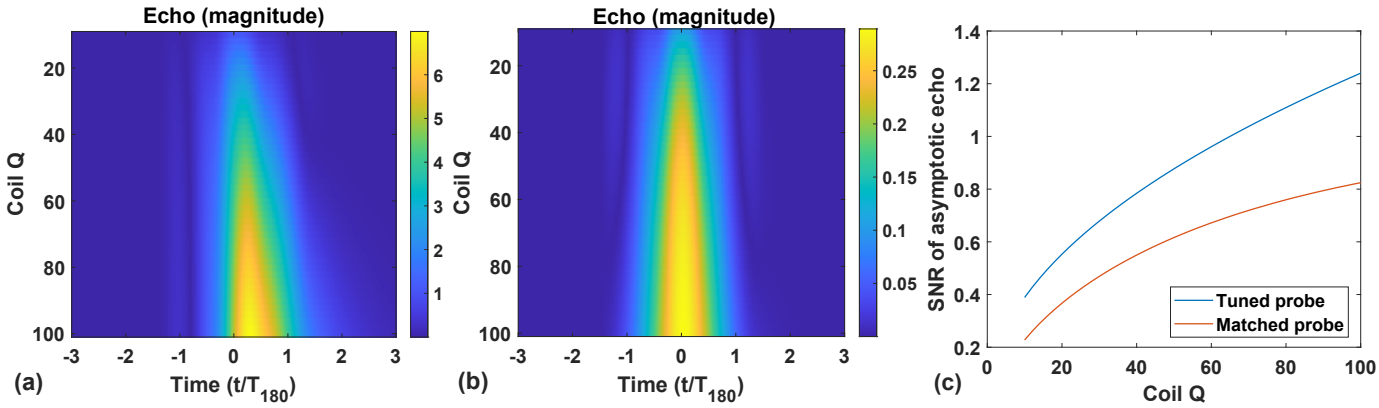

Figure 13: Simulated asymptotic echo shapes for CPMG sequences in a linear B_0 field gradient and uniform B_1 as a function of coil Q for: (a) a tuned probe, and (b) a matched probe. (c) Signal-to-noise ratio (SNR) in voltage units for the two cases. The following probe and pulse sequence parameters were used: $L = 10$ μH, $Q = [10-100]$, $[R_{s,on}, R_{s,off}] = [2, 20]$ Ω (tuned probe) or $R_s = 50$ Ω (matched probe), $\omega_0 = 2\pi \times 1$ MHz, $\omega_{1,max} = 2\pi \times 10$ kHz (such that $T_{90} = 25$ μs and $\omega_{1n} = [0.1 - 1]$), $T_{180} = 2 \times T_{90}$, and $T_{acq} = 3 \times T_{180}$.

In the earlier simulations, we assumed that the probe tuning (or impedance-matching) frequency ω_r was equal to both the nominal RF frequency, ω, and the average Larmor frequency of the sample, ω_0. Here we study the effects of probe tuning error, i.e., non-zero offset $\Delta\omega_r = (\omega - \omega_r)$. In particular, we assume that $\Delta\omega_r$ (normalized to the nominal probe bandwidth of ω_r/Q) varies over the $[-5, 5]$ range. The resulting asymptotic magnetization spectra $S_{rx}(\omega)$ are shown in Figs. 14(a)-(b) for tuned and matched probes, respectively, while Fig. 14(c) summarizes the SNR obtained from the two designs. The

figure shows that in both cases the received signal amplitude decreases as $\Delta\omega_r$ increases, as expected. The signal gain of the matched probe is more robust to mis-tuning since it has about 2× more −3 dB bandwidth. However, the SNR of the matched probe degrades much more quickly with mis-tuning; this is because its NF is a much stronger function of $\Delta\omega_r$, as shown in Fig. 10(b). Thus, the high signal gain of the tuned probe, which minimizes its NF, also makes its SNR more robust to mis-tuning.

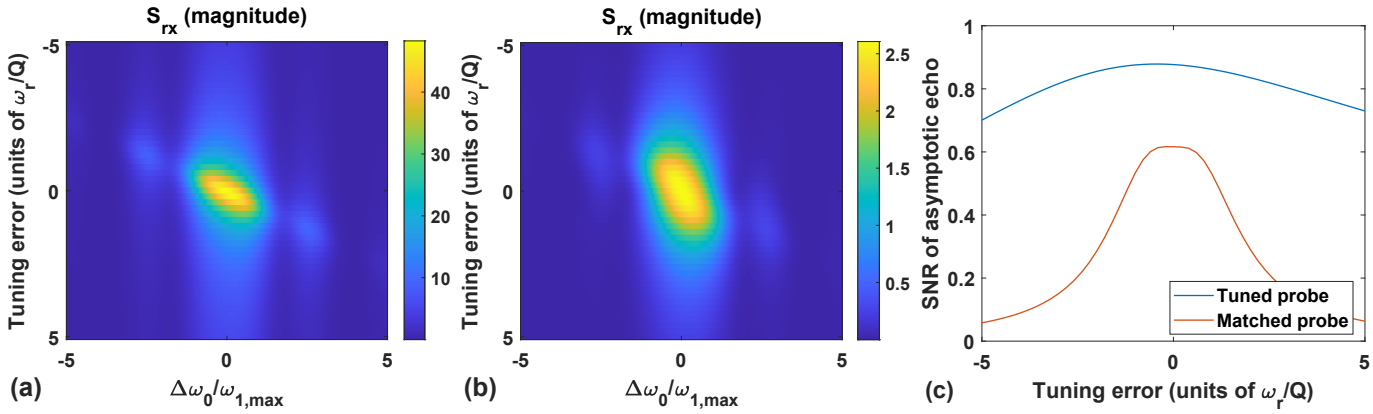

Figure 14: Simulated asymptotic received spectrum S_{rx} for CPMG sequences in a linear B_0 field gradient and uniform B_1 as a function of probe tuning error $\Delta\omega_r$ for: (a) a tuned probe, and (b) a matched probe. (c) Signal-to-noise ratio (SNR) in voltage units for the two cases. Probe and pulse sequence parameters are identical to those in Fig. 13, apart from fixed coil $Q = 50$ (such that $\omega_{1n} = 0.5$).

6.4. CPMG-Like Sequences using SPA Refocusing Pulses

This section analyzes the effects of probe dynamics on CPMG-like sequences that use broadband SPA refocusing pulses to improve SNR. In particular, we consider the SPA pulses of various lengths described in [29], which were numerically optimized without including any probe-related effects. For convenience, we denote these pulses as SPA_x where x is the normalized pulse length (in units of $T_{180} = \pi/\omega_1$). It is also known that phase or amplitude modulation is not beneficial for short refocusing pulses with $x < 1$, so we use nominally-rectangular pulses (denoted by Rect_x) in this case.

Fig. 15 summarizes the asymptotic SNR provided by CPMG-like pulse sequences as a function of refocusing pulse length (t_{ref}) for untuned, tuned, and matched probes when $\omega_{1n} \ll 1$ and probe dynamics effects are expected to be negligible. A short nominally-rectangular excitation pulse (normalized amplitude $k = 6$, length $t_{exc} = T_{90}/6$) was used to generate broadband initial magnetization $\vec{M}_{exc}$. The figure shows that longer SPA pulses ($t_P > T_{180}$) provide up to 2× higher SNR (in rms units) than the

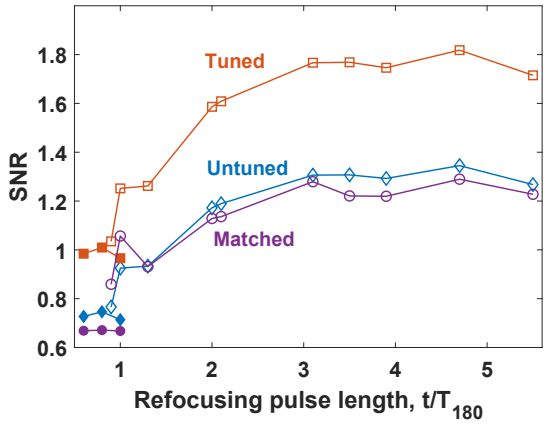

Figure 15: Asymptotic SNR of CPMG-like pulse sequences for untuned, tuned, and matched probes as a function of refocusing pulse length t_{ref} when $\omega_{1n} \ll 1$, such that probe dynamics effects are small. Filled and open symbols correspond to rectangular and SPA refocusing pulses, respectively; a short nominally-rectangular excitation pulse ($t_{exc} = T_{90}/6$) was used in both cases. The following probe and pulse sequence parameters were assumed: $L = 1.25$ μH, $Q = 50$, $[R_{s,on}, R_{s,off}] = [2, 20]$ Ω (tuned probe) or $R_s = 50$ Ω (matched probe), a uniform B_0 gradient around $\omega_0 = 2\pi \times 8$ MHz, $\omega_{1,max} = 2\pi \times 10$ kHz (such that $T_{90} = 25$ μs and $\omega_{1n} = 0.0625$), $t_E = t_{ref} + 6 \times T_{180}$, and $T_{acq} = 4 \times T_{180}$.

default refocusing pulses (nominally-rectangular with $t_{ref} = 1 \times T_{180}$). Also, the relative amount of SNR improvement is similar for all three probes, as expected in the absence of probe dynamics effects. However, the tuned probe provides the highest absolute SNR due to its lower NF in receive-mode, as described in the previous section.

Next, we simulate the same CPMG-like sequences for different values of normalized RF bandwidth ω_{1n}. In addition to SNR, we define and plot two additional performance metrics that are relevant for low-field experiments in inhomogeneous fields, such as single-sided imaging [44]. The first, the time figure of merit (FOM$_t$), is inversely proportional to the total time required to obtain a certain "target" SNR. Since SNR $\propto \sqrt{N_{av}}$ where N_{av} is the number of scans being averaged, FOM$_t$ $\propto$ (SNR)^2. In addition, the SNR per scan for amplitude and T_2 measurements is $\propto 1/t_E$ where t_E is the echo period, since smaller values of t_E allow more echoes to be generated per scan. Including this term, we get $FOM_t \equiv$ (SNR)$^2/t_E$, where larger values are better. The second metric, the energy figure of merit (FOM$_e$), is inversely proportional to the total RF energy required to obtain a certain SNR. Since all SPA and rectangular pulses have the same nominal RF amplitude, the energy per pulse is $\propto t_{ref}$, the pulse length. Thus, we get $FOM_e \equiv$ (SNR)$^2/(t_E t_{ref})$, where larger values are again better.

The simulation results are summarized in Fig. 16 for ω_{1n} values ranging from 0.0625 to 2. Each plot

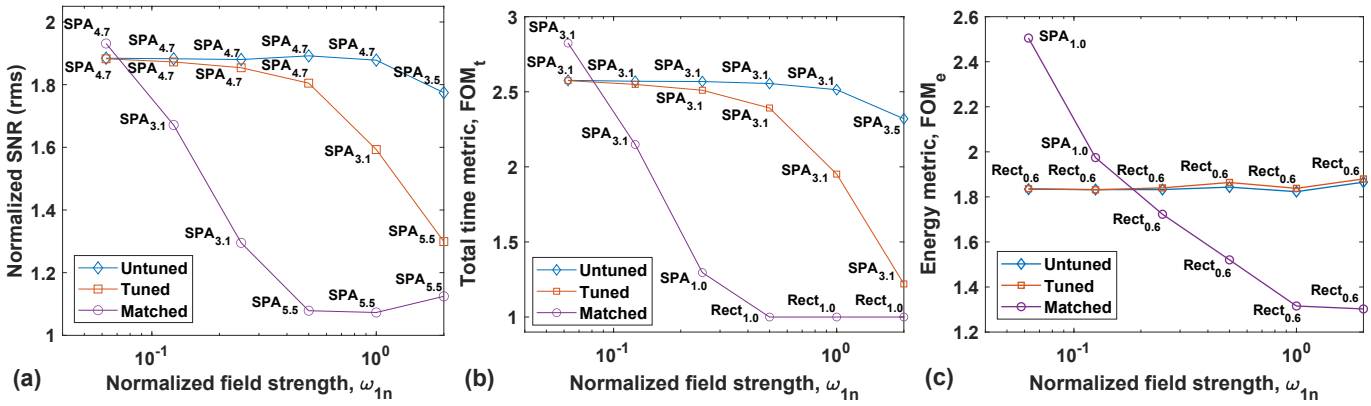

Figure 16: Summary of probe dynamics effects on CPMG-like pulse sequences generated by untuned, tuned, and matched probes as a function of normalized field strength ω_{1n} (obtained by varying ω_r while keeping ω_1 and coil Q fixed). The plots show the refocusing pulses that optimize the following metrics: (a) asymptotic SNR, (b) inverse of total measurement time FOM$_t$, and (c) inverse of total measurement energy FOM$_e$. All metrics have been normalized to values for nominally-rectangular refocusing pulses ($t_{ref} = 1 \times T_{180}$) at the same value of ω_{1n}. Probe and pulse sequence parameters are identical to those in Fig. 15, except the following: $\omega_r = \omega_0 = 2\pi \times [0.25 - 8]$ MHz and coil inductance $L = 10 \times (2\pi \times 10^6/\omega_0)$ μH.

shows the best available value of a given performance metric (SNR, FOM$_t$, and FOM$_e$ for Figs. 16(a)-(c), respectively) as a function of ω_{1n}, and also the corresponding refocusing pulse (either SPA or nominally-rectangular). All values have been normalized to those from the default Rect$_{1.0}$ pulse. These plots highlight some interesting trends. The SNR plot (Fig. 16(a)) shows that the normalized SNR (i.e., the improvement relative to the Rect$_{1.0}$ pulse) decreases with ω_{1n} for all three probe designs. However, the effect is weak for the untuned probe (since it is broadband in both transmit and receive), intermediate for the tuned probe (since it is broadband in transmit, narrowband in receive), and strongest for the matched probe (since it is narrowband in both transmit and receive). Also, relatively long SPA pulses ($t_{ref} \geq 3.1 \times T_{180}$) provide the best SNR in all cases, as expected from Fig. 15.

The FOM$_t$ plot (Fig. 16(b)) shows that measurement time increases with ω_{1n} for all three probes, i.e., as probe dynamics effects become more significant. Again, the effect is weakest for untuned probes and strongest for matched ones. The SPA$_{3.1}$ pulse always maximizes FOM$_t$ for untuned and tuned probes, but the nominally-rectangular Rect$_{1.0}$ pulse is optimal for matched probes at high values of ω_{1n}. This is because of the relatively slow RF rise and fall times in matched probes, which prevents modulated pulses (such as SPA) from being accurately generated as ω_{1n} increases.

Finally, the FOM$_e$ plot (Fig. 16(c)) shows that short nominally-rectangular pulses (Rect$_{0.6}$) generally minimize the total energy consumption. The only exception is matched probes at low values of ω_{1n},

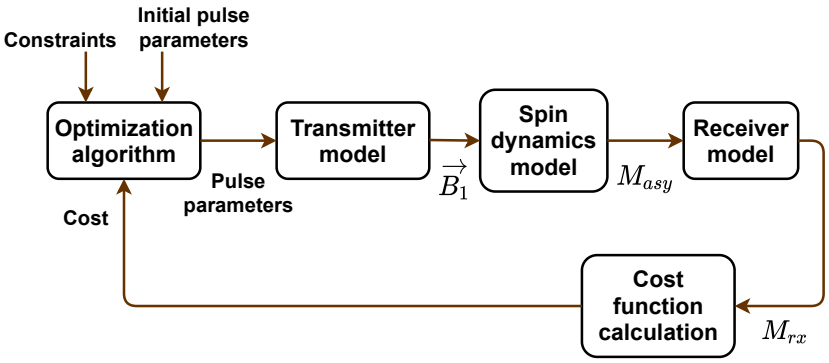

Figure 17: Block diagram of the proposed hardware-aware RF pulse optimization procedure.

for which a relatively short SPA pulse ($\text{SPA}_{1.0}$, which is similar to the RP2 pulse described in [27]) is optimal. Also, the normalized value of FOM_e is nearly independent of ω_{1n} for untuned and tuned probes, but decreases with ω_{1n} for matched probes (which shows that the $\text{Rect}_{1.0}$ pulse becomes closer to optimal).

Returning to Fig. 16(a), note that while the highest value of *normalized* SNR is always obtained for small values of ω_{1n} (i.e., when ω_1 is much smaller than the probe bandwidth), this does *not* imply that ω_1 should be reduced to improve the measurement SNR. On the contrary, matched filtering ensures that the effective sample volume (and thus SNR) in inhomogeneous fields is maximized by using the largest available ω_1. Fig. 16(a) simply shows that the *relative* improvement in SNR that is possible by using SPA pulses tends to increase as ω_{1n} decreases, i.e., as probe dynamics effects become less significant. In other words, the optimal choice of pulse for a given value of ω_1 depends on the nominal probe bandwidth ω_r/Q. Similar remarks apply for the other metrics (FOM_t, and FOM_e).

6.5. Design of OCT Pulses for CPMG-Like Pulse Sequences

In this section we describe the design of excitation and refocusing pulses for CPMG-type sequences that are optimized for different probe designs. For this purpose, we integrated our models for the transmitter, spin dynamics, and receiver within an OCT framework as shown in Fig. 17.

Eqn. (27) shows that the asymptotic magnetization spectrum $S_{asy}(\Delta\omega_0)$ for a given field distribution $f(\Delta\omega_0, \omega_1)$ is proportional to the inner product $(\hat{n} \cdot \vec{M}_{exc})$, where $\vec{M}_{exc}$ and $\hat{n}$ are solely determined by the excitation pulse and refocusing cycle, respectively. Thus, we optimize the excitation and refocusing

pulses separately, as in our earlier work [27–29]. Our goal is to maximize measurement SNR for a given peak RF power level (i.e., value of $\omega_{1,max}$). The specific optimization steps are described next.

6.5.1. Refocusing pulses

The received signal spectrum can be found by including the receiver TF in eqn. (27), resulting in $S_{rx}(\Delta\omega_0) = G_R(\Delta\omega_0)S_{asy}(\Delta\omega_0)$. The magnitude of $S_{asy}(\Delta\omega_0)$ is maximized for ideal axis-matching excitation (AMEX) pulses that transfer $\hat{z} \rightarrow \hat{n}$, thus generating $\vec{M}_{exc} = \hat{n}$ at all offset frequencies [28]. In this case, the expression for the received spectrum reduces to

$$S_{rx}^{(\mathrm{AMEX})}(\Delta\omega_0) = G_R(\Delta\omega_0)\,(\omega_0 + \Delta\omega_0)\int f(\Delta\omega_0, \omega_1)\hat{n}_\perp \omega_1 d\omega_1. \tag{29}$$

We denote the resulting SNR for asymptotic echoes by $\mathrm{SNR}^{(\mathrm{AMEX})}$. By contrast, traditional broadband excitation pulses (such as the short nominally-rectangular pulses used in the previous section), ideally transfer $\hat{z} \rightarrow n_x$ within the refocusing bandwidth; this results in lower SNR.

Refocusing pulses were discretized into M fixed-length segments (each of length $\Delta T = 2\pi/\omega$, i.e., one RF cycle) for optimization purposes. The transmitter voltage waveform for the m-th segment was assumed to have an arbitrary phase $\phi_{in}(m)$, while the transmitter voltage amplitude V_s was kept constant during the pulse to i) simplify the optimization problem, and ii) allow the optimized pulses to be easily generated by power-efficient switching power amplifiers. Thus, the optimization variables consist of the M-element list of input phases, which in turn determine $\hat{n}_\perp$ in eqn. (29). The field distribution $f(\Delta\omega_0, \omega_1)$ was assumed to be constant, and $-SNR^{(\mathrm{AMEX})}$ was chosen as the cost function.

Optimized pulse shapes with a nominal length of $t_{ref} = 1.5 \times T_{90}$ are shown in Figs. 18(a), (c), and (e) for untuned probes ($\omega_{1n} = 1$), tuned probes ($\omega_{1n} = 1$), and matched probes ($\omega_{1n} = 0.5$), respectively[6], while the corresponding asymptotic magnetization spectra (S_{asy} and S_{rx}) are shown in Figs. 18(d), (e), and (f). The rate of phase modulation within the pulse is highest for the untuned probe and lowest for the matched probe, as expected. The pulse optimized for tuned probes (Fig. 18(c)) is similar to a phase-alternating approximation to a swept-frequency pulse, while that for matched probes (Fig. 18(c))

[6] A smaller value of ω_{1n} was used for matched probes due to their significantly slower pulse rise and fall times.

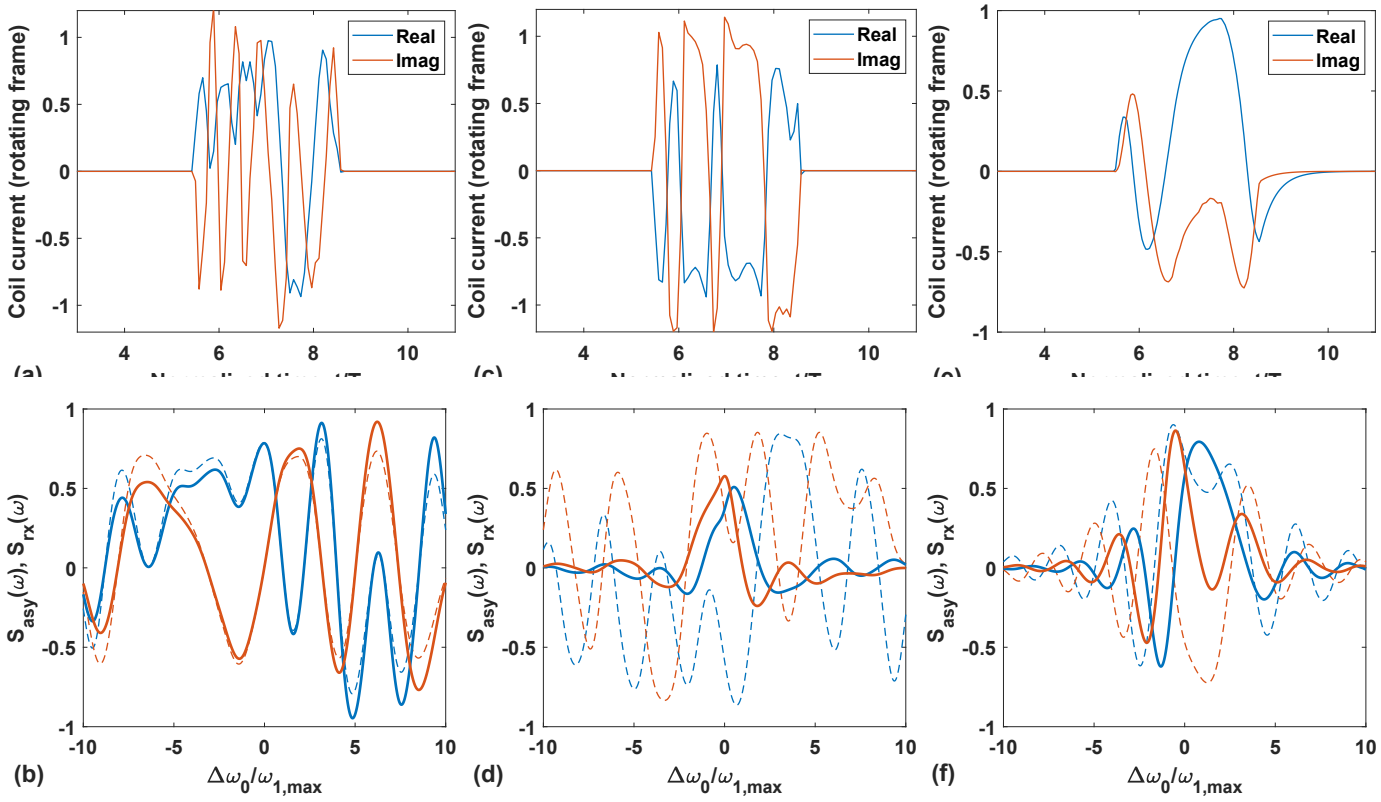

Figure 18: Optimized refocusing pulses in a linear B_0 field gradient and uniform B_1 for (a)-(b) an untuned probe, (c)-(d) a tuned probe, and (e)-(f) a matched probe. In each case, the top plot shows coil current in the rotating frame, while the bottom plot shows asymptotic magnetization spectra at the coil ($S_{asy}(\omega)$, dashed lines) and the receiver ($S_{rx}(\omega)$, solid lines). For clarity, $S_{rx}(\omega)$ was divided by the peak receiver gain $|G_R(\omega)|_{\max}$. Probe and pulse sequence parameters were as follows: $L = 10$ μH, $Q = 50$, $[R_{s,on}, R_{s,off}] = [2, 20]$ Ω (tuned probe) or $R_s = 50$ Ω (matched probe), $\omega_r = \omega_0 = 2\pi \times 0.5$ MHz, $\omega_{1,max} = 2\pi \times 10$ kHz (such that $T_{90} = 25$ μs and $\omega_{1n} = 1$), pulse length $t_P = 1.5 \times T_{180}$, and $T_{acq} = 3 \times T_{180}$.

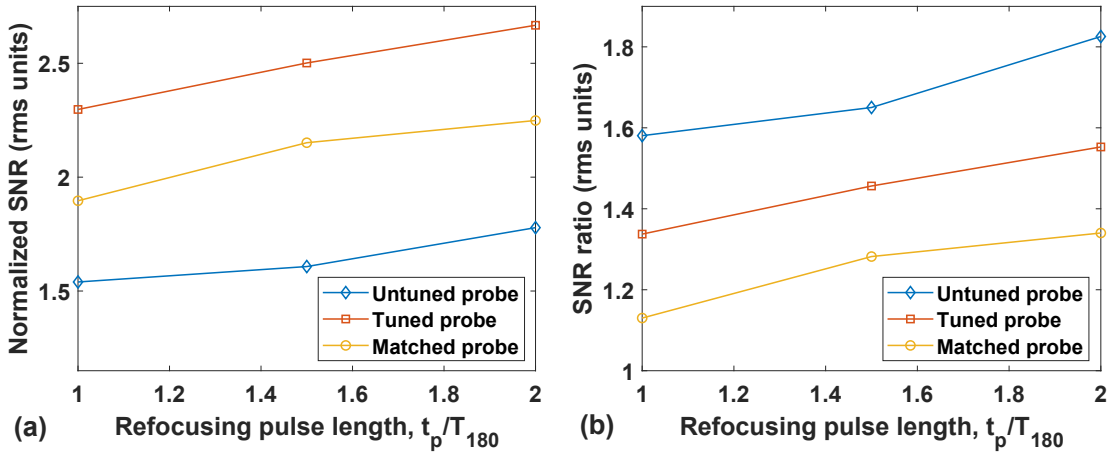

Figure 19: Refocusing pulse optimization results for untuned, tuned, and matched probes in a uniform B_0 gradient at $\omega_r = \omega_0 = 2\pi \times 500$ kHz: (a) normalized SNR for asymptotic echoes, and (b) relative SNR compared to rectangular input pulses of length $1.6 \times T_{90}$. Coil parameters are identical to those in earlier sections, while $\omega_{1,max} = 2\pi \times 10$ kHz ($T_{90} = 25$ μs, $\omega_{1n} = 1$) for tuned and untuned probes and $2\pi \times 5$ kHz ($T_{90} = 50$ μs, $\omega_{1n} = 0.5$) for the matched probe.

is similar to a three-segment SPA or RP2 pulse. Both untuned and tuned probes generate significant amounts of off-resonance magnetization (S_{asy}), but S_{rx} for the latter is significantly more narrowband due to the resonant receive-mode TF. Finally, both S_{asy} and S_{rx} are narrowband for the matched probe.

The optimization procedure was repeated for t_{ref} varying between T_{180} and $2 \times T_{180}$. The resulting SNR values are summarized in Fig. 19(a) for untuned, tuned, and matched probes with the same values of ω_{1n} as before (1, 1, and 0.5, respectively). The results show that SNR increases with t_{ref}, as expected, and is highest for tuned probes due to their low receive-mode NF. Fig. 19(b) shows the same data, but normalized to the SNR provided by the default nominally-rectangular pulse ($\text{Rect}_{1.0}$). These results show that the relative amount of SNR improvement is lowest for matched probes, intermediate for tuned probes, and highest for untuned probes, as expected based on their dynamics. For example, optimized pulses with $t_{ref} = 2 \times T_{180}$ can provide approximately 40%, 60%, and 80% higher SNR than the default pulse, respectively, resulting in FOM_t improvements of approximately 1.6×, 2.5×, and 3.2×.

6.5.2. Excitation pulses

A similar procedure was used for optimizing AMEX excitation pulses. The main difference is that the asymptotic signal spectrum is given by eqn. (27), with $\vec{M}_{exc}$ varying during the optimization while $\hat{n}$ and $\hat{n}_\perp$ remain fixed at values corresponding to one of the optimized refocusing pulses described in the

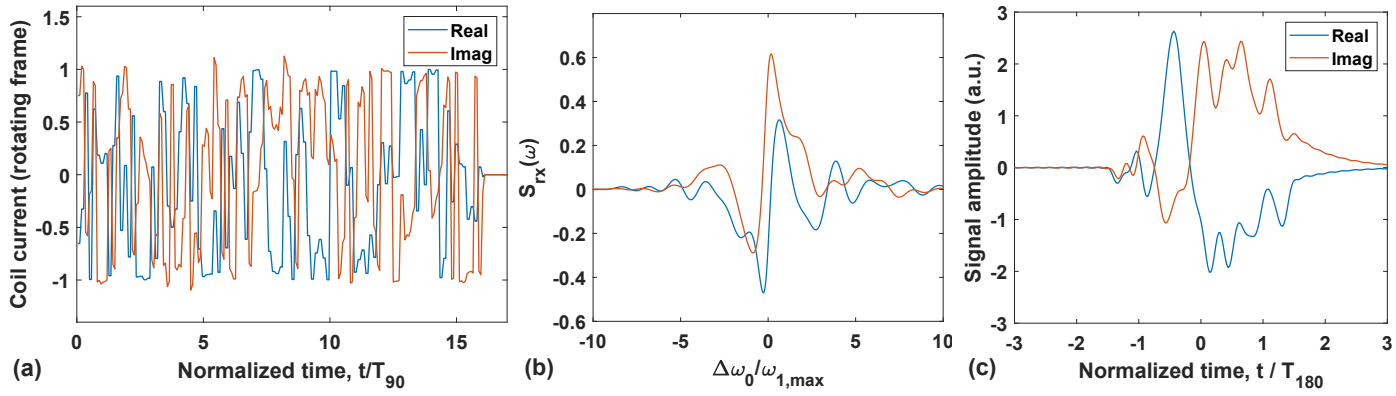

Figure 20: Optimized AMEX pulse sequence in a uniform B_0 gradient for a tuned probe at $\omega_r = \omega_0 = 2\pi \times 500$ kHz: (a) coil current for the excitation pulse in the rotating frame (length $t_{exc} = 8 \times T_{180}$), (b) received magnetization spectrum $S_{rx}(\omega)$, and (c) asymptotic time-domain echo. The AMEX excitation pulse was matched to the broadband refocusing pulse of length $t_P = 1.5 \times T_{180}$ shown in Fig. 18(c), with $t_E = 7 \times T_{180}$. Coil parameters are identical to those in earlier sections. The value of $\omega_{1,max} = 2\pi \times 10$ kHz (such that $T_{90} = 25$ μs and $\omega_{1n} = 1$).

previous section. The pulse was again discretized into fixed-length segments (each of length $\Delta T = 4\pi/\omega$, i.e., two RF cycles), and $-SNR$ was chosen as the optimization cost function. The pulse length was chosen to be slightly larger than the echo period t_E, namely $t_{exc} = 8 \times T_{180}$ when $t_E = 7 \times T_{180}$. This is because AMEX pulses need to be comparable or longer than t_E to generate a $\vec{M}_{exc}$ vector that matches $\hat{n}$ (which is approximately periodic with a period $1/t_E$), Finally, during this step we only considered tuned probes (with $\omega_{1n} = 1$) for conciseness.

Fig. 20(a) shows an optimized AMEX pulse that is matched to the previously-optimized refocusing pulse ($t_{ref} = 1.5 \times T_{180}$) for an echo period $t_E = 7 \times T_{180}$. We denote the resulting CPMG-like pulse sequence as $\text{AMEX}_{1.5}$. Figs. 20(b) and (c) show the corresponding asymptotic magnetization spectrum (S_{rx}) and time-domain echo, respectively.

The optimization procedure was repeated for refocusing pulses of lengths between T_{180} and $2 \times T_{180}$. The optimized SNR values were normalized to those from the default CPMG sequence, which uses nominally-rectangular excitation and refocusing pulses ($t_{exc} = T_{90}$, $t_{ref} = 1.6 \times T_{90}$)[7]. The normalized SNR is up to 65% higher than the default sequence (resulting in 2.7× lower FOM_t), as shown in Fig. 21(a). These results show that OCT-based pulse optimization can significantly improve measure-

[7]A value of $t_{ref} = 1.6 \times T_{90}$ was chosen since it provides slightly higher SNR in a grossly inhomogeneous field than the more common $t_{ref} = 2 \times T_{90}$ (see Fig. 15).

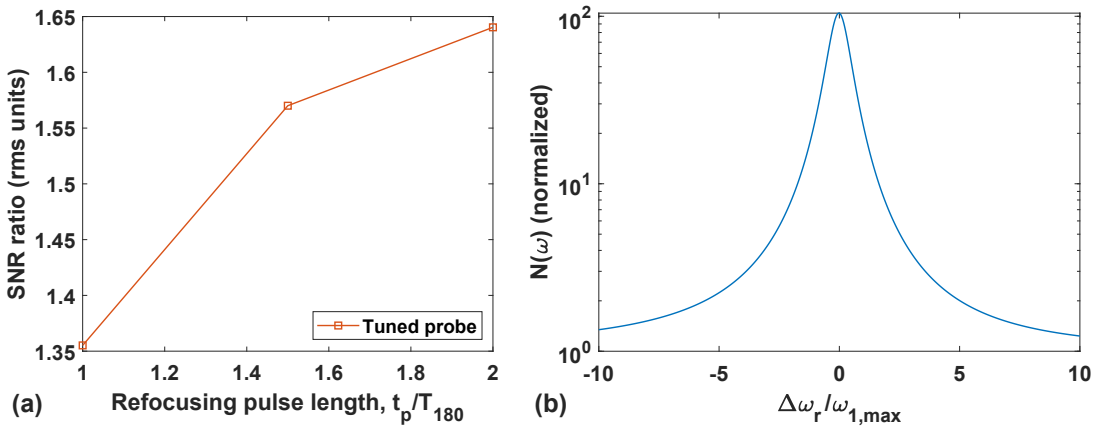

Figure 21: (a) Summary of CPMG optimization results for a tuned probe in a uniform gradient at $\omega_r = \omega_0 = 2\pi \times 500$ kHz. The figure shows relative improvement in asymptotic SNR for AMEX pulse sequences (echo period $t_E = 7 \times T_{180}$) compared to a CPMG sequence that uses rectangular input pulses ($t_{exc} = T_{90}$, $t_{ref} = 1.6 \times T_{90}$). (b) The corresponding PSD, $N(\omega)$, of total input-referred noise at the receiver. Coil parameters are identical to those in earlier sections. The value of $\omega_{1,max} = 2\pi \times 10$ kHz (such that $T_{90} = 25$ μs and $\omega_{1n} = 1$).

ment metrics (such as SNR and FOM_t) even when probe dynamics effects are significant ($\omega_{1n} = 1$),

Interestingly, much of the improvement is due to using $H'_M(\omega)$, the optimal matched filter for colored (i.e., frequency-dependent) noise. The noise power spectrum $N(\omega)$ of high-Q tuned probes is strongly frequency-dependent, as shown in Fig. 21(b); the peak near the tuning frequency is due to resonant amplification of noise from the coil. As a result, $H'_M(\omega)$ provides higher SNR than $H_M(\omega)$, the matched filter for white noise. This effect is much stronger for the AMEX sequence since it generates much more off-resonance magnetization. For example, using the correct filter increases the SNR of the $\text{AMEX}_{1.5}$ sequence by 81%, compared to only 14% for the default sequence.

6.5.3. Phase cycling

An important practical concern with pulse sequences based on OCT pulses is their support of phase cycling, which is very useful for i) selecting the desired coherence pathways, and ii) removing unwanted signals due to steady-state magnetization, probe ring-down, and detector offset. Standard phase cycles use a π phase shift of the excitation pulse to invert $\vec{M}_{exc}$, but in fact this inverts only the transverse component of the vector. As a result, only this component contributes to the signal after the phase cycle. Since AMEX pulses deliberately create both transverse and longitudinal magnetization, generalized phase cycling of AMEX pulses requires a method to invert both components of $\vec{M}_{exc}$. In general,

this requires two matched AMEX excitation pulses that transform $\hat{z}$ magnetization onto $\hat{n}$ and $-\hat{n}$, respectively. In the special case of SPA refocusing pulses, a modified form of phase cycling, known as phase inversion, can be applied to the corresponding AMEX pulses; this is because the asymptotic magnetization is symmetric about $\Delta\omega_0 = 0$ [29]. However, the proposed hardware-optimized refocusing pulses are not of the SPA type, so phase inversion does not apply.

Thus, here we use our optimization framework to design inverse excitation pulses. Such pulses generate initial magnetization vectors $\vec{M}_{exc}$ and asymptotic magnetization spectra $S_{rx}(\Delta\omega_0)$ that are, ideally, additive inverses of those produced by a previously-optimized AMEX pulse. Basic phase cycling can then be performed by subtracting the signals generated by pairs of scans that use the same refocusing cycle but the original and inverse AMEX pulses, respectively; this is similar to the phase-alternating pair (PAP) cycle. Given an AMEX pulse, its inverse was found by minimizing the cost function

$$C = \int d\left(\Delta\omega_0\right) \left| S_{rx}\left(\Delta\omega_0\right) + S_{rx,orig}\left(\Delta\omega_0\right) \right| + \alpha \left| SNR - SNR_{orig} \right|, \tag{30}$$

where 'orig' subscripts refer to the original pulse and α is a constant. The first term ensures that the magnetization spectra are inverses of each other, while the second term prevents the optimizer from getting stuck in local optima that have poor asymptotic SNR.

For this step, we used the same probe model as that in the previous sub-section (tuned, $\omega_{1n} = 1$). Optimization results for an $\text{AMEX}_{1.0}$ sequence are shown in Fig. 22. Both the asymptotic magnetization spectrum and time-domain echo are nearly perfect inverses of the original (correlation coefficient $\rho = -0.998$), as desired. Interestingly, the fact that the spin dynamics are nonlinear ensures that the waveforms of the original and inverse excitation pulses have no simple relationship to each other: the actual coil currents are almost completely uncorrelated ($\rho = 0.04 + 0.03i$). The inverted pulses do tend to have slightly lower SNR than the original pulses (9.7% in this case), resulting in a small drop in SNR after phase cycling. The value of α in the cost function (eqn. 30) can be increased to reduce this drop.

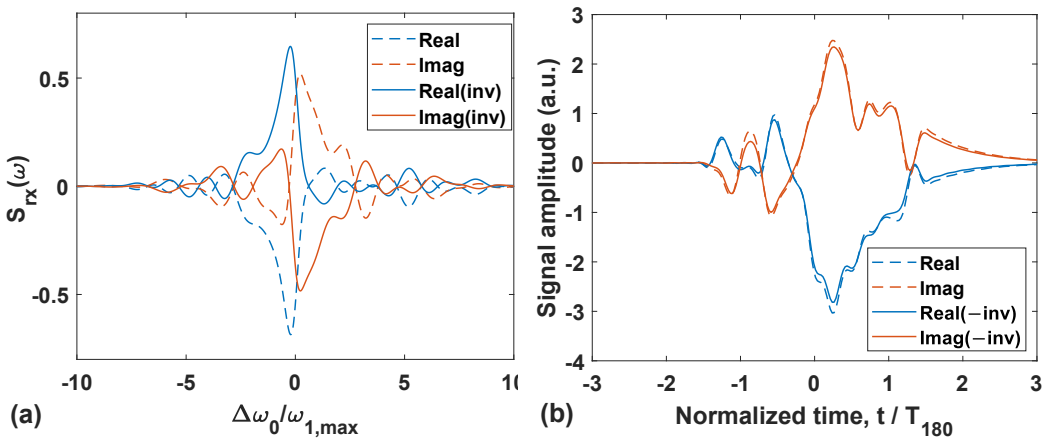

Figure 22: Performance of an optimized inverse AMEX pulse sequence compared with the original: (a) received magnetization spectra $S_{rx}(\omega)$ (dashed: original sequence, solid: inverse sequence), and (b) asymptotic time-domain echoes (dashed: original sequence, solid: negative of the inverse sequence). The AMEX excitation pulses were matched to a broadband refocusing pulse of length $t_P = 1 \times T_{180}$, with $t_E = 7 \times T_{180}$. Coil parameters are identical to those in earlier sections. The values of $\omega_r = \omega_0 = 2\pi \times 500$ kHz and $\omega_{1,max} = 2\pi \times 10$ kHz (such that $T_{90} = 25$ μs and $\omega_{1n} = 1$).

7. Experimental Results

This section describes some experiments using an untuned transmitter and probe to verify our transient cancellation results (described in Section 2). The system, which has been described elsewhere [8], consists of a broadband "H-bridge transmitter" that drives an untuned solenoid coil containing the sample. The duplexer and receiver electronics were not used during the experiments.

Constant-amplitude RF pulses were fed into the transmitter from a Kea2 benchtop spectrometer (Magritek). The transmitter contains circuitry that converts these low-level pulses (< 0 dBm) into logic-level drive signals for the MOSFET switches in the H-bridge. The resultant coil current was measured with a current probe and displayed on a digital oscilloscope. Typical results obtained with rectangular input pulses at 250 kHz are shown in Fig. 23(a). The second pulse displays turn-on and turn-off transients; the former is well-fit by an exponential decay with time-constant $\tau_p = 6.0$ μs, as shown on the figure. The untuned probe model in Section 2 predicts $\tau_p = L/(R_c + R_{s,on})$, which agrees with the measurement given that $L = 15$ μH, $R_c \approx 0.5$ Ω, and $R_{s,on} \approx 2.0$ Ω.

Interestingly, the turn-off transient is noticeably non-exponential - in fact, it is approximately linear. This is because no resistive "Q-switch" was used after the pulse turns off, unlike in our analysis (shown in Fig. 2(b)). Instead, the inductor current discharges through extender and MOSFET source-drain

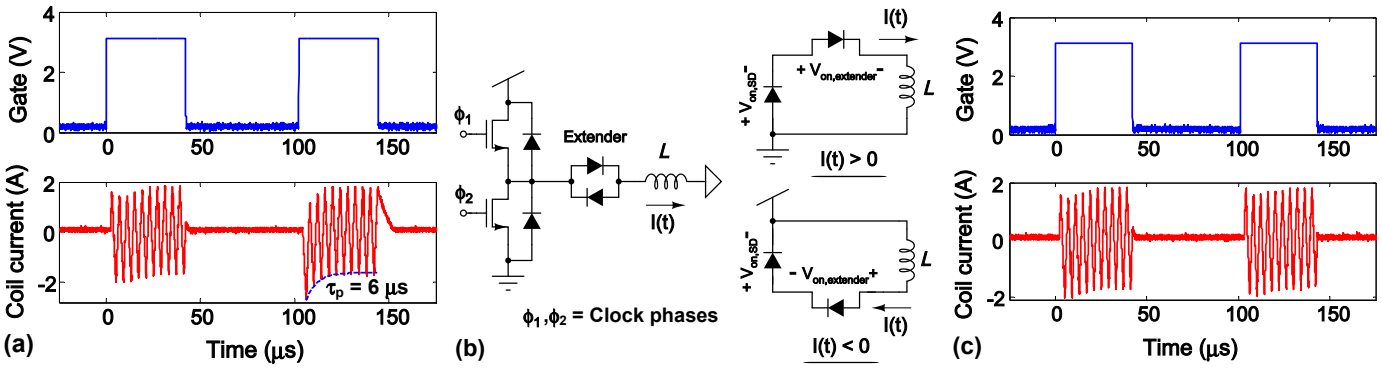

Figure 23: (a) Measured coil currents produced by an untuned NMR transmitter at 250 kHz. The transmitter voltage was set to 30 V. The input consisted of two rectangular (constant amplitude and phase) RF pulses, each 40 μs long. Pulse locations are indicated by the "gate" pulses shown above each current waveform. (b) Simplified schematic of the untuned NMR transmitter and probe (left), and its equivalent circuit during pulse ring-down (right). For simplicity, the differential transmitter and probe circuit has been split into two parts down its axis of symmetry (the center of the coil), and only one of the two half-circuits is shown. (c) Same as (a), but with the second pulse delayed by 1 μs.

reverse diodes, as shown in Fig. 23(b). This process (known as "free-wheeling") can be modeled by assuming that the voltage across each diode remains constant at its "on" value. This results in a linear decrease in coil current, in good agreement with the measurements:

$$L\frac{dI}{dt} = V \approx -V_{on} \Rightarrow I(t) = I(0) - \left(\frac{V_{on}}{L}\right)t, \tag{31}$$

where $V_{on} = 2\left(V_{on,SD} + V_{on,extender}\right)$ is the total diode voltage. The factor of two appears because of the other half of the H-bridge circuit (not shown in Fig. 23(b)).The measured slope of the coil current during turn-off is 0.21 A/μs, which corresponds to $V_{on} = 3.15$ V. This result is in good agreement with the predicted value of $V_{on} \approx 3.4$ V.

Fig. 23(c) shows that both turn-on and turn-off transients disappear when the second pulse is delayed by 1 μs, i.e., one quarter of an RF cycle. In addition, the amplitude of the transient varies periodically as the delay is further increased. The observed period is half of an RF cycle (2 μs in this case), as predicted by the theoretical analysis.

In the next set of experiments, we generated SPA pulses with three segments at a frequency at 500 kHz. Fig. 24(a) shows that large transients are generated at the beginning and end of each pulse, as well as every time the phase changes within a pulse. Fig. 24(b) shows that these transients disappear

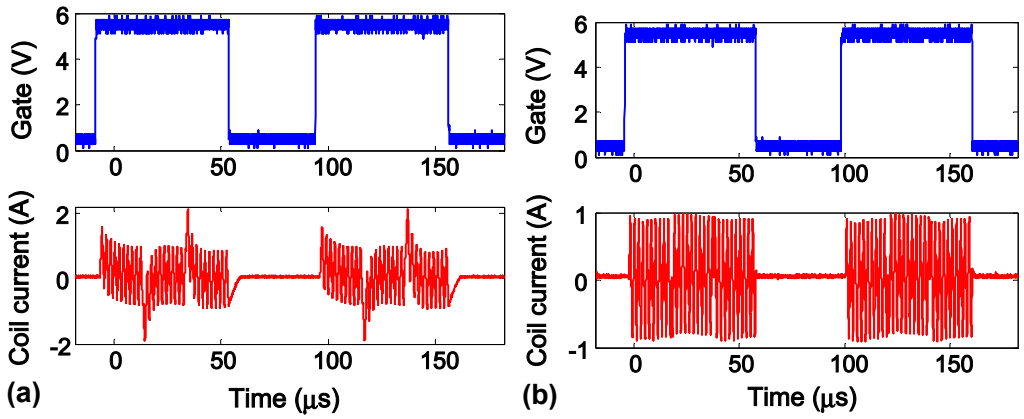

Figure 24: Measured coil currents produced by an untuned NMR transmitter at 500 kHz. The transmitter voltage was set to 30 V. The input consisted of two constant-amplitude SPA pulses, each 60 μs long. Each pulse consisted of 3 segments of length 20 μs, with phases of $\{0, \pi, 0\}$, respectively. Pulse locations are indicated by the "gate" pulses shown above each current waveform. (a) Using default delay settings. (b) Same as (a), but with the initial delay increased by 0.5 μs.

when the delay before the first pulse is increased by 0.5 μs, i.e., one quarter of an RF cycle. Further examination of the resulting pulse waveform confirms that all phase transitions occur at zero-crossings of the coil current, as required by the theoretical analysis for phase jumps of $\pm\pi$. In addition, the amplitude of the transient again repeats periodically with a period of half an RF cycle (1 μs in this case) as the delay is further increased.

8. Summary and Conclusions

This paper has analyzed the effects of limited probe bandwidth on multi-pulse measurements on ensembles of uncoupled spin-1/2. To simplify the analysis, we have created analytical models of three common probe circuits, referred to as untuned, tuned, and impedance-matched, respectively. Our analytical and simulation results show that the dynamics of untuned probes during transmission can be suppressed using careful timing of the phase transitions. Such behavior can also be approximated using tuned probes that are over-coupled (i.e., use low-impedance transmitters), but it cannot be obtained using matched probes. In receive-mode, untuned probes exhibit a broadband TF, while the others have resonant (narrowband) TFs. The resulting signal gain (assuming moderate- or high-Q coils) is much larger for tuned probes than the others, which results in the lowest NF and highest SNR as long as transmission-line effects between the probe and receiver can be ignored.

The probe models were integrated with spin dynamics simulations to study their effects on measurement metrics such as SNR. Our results show that these effects increase with normalized RF bandwidth ω_{1n}, and are generally weakest for untuned probes, intermediate for tuned probes, and strongest for matched probes. Finally, the models were incorporated into an OCT pulse optimization framework and used to derive hardware-specific excitation and refocusing pulses for CPMG-like pulse sequences in grossly inhomogoeneous fields. The results show that the optimized pulses can significantly improve SNR and other metrics even when probe dynamics effects are significant.

Future work will focus on verifying our pulse sequence optimization results on suitable probe hardware. We would also like to extend our theoretical analysis to additional probe circuits, such as balanced and transmission-line designs. Finally, we will also study the impact of probe dynamics on pulse designs for studying coupled networks of spins, such as pulses for decoupling and sub-spectral editing.

Acknowledgments

The authors would like to thank Shin Utsuzawa for helpful discussions.

Appendix A. General Solution for Transient Cancellation in Untuned Probes

The general solution for the resulting non-sinusoidal coil current can be found by replacing the driving function in eqn. (4) with a Fourier series

$$f(t) = u(t) \sum_{n=1}^{\infty} a_n e^{in(\omega t + \phi)}, \tag{A.1}$$

where the coefficients a_n depend on the transmitter voltage waveform. Note that we have implicitly assumed that the average (DC) term is zero by starting the series from $n = 1$. Using superposition, the

general solution for the coil current is now given by

$$
\begin{aligned}
y(t) &= y_h(t) + \left(y_{d1}(t) + y_{d2}(t)\right)/2. \qquad \text{(A.2)}\\
&= y(0)e^{-t/\tau_p} + u(t)\sum_{n=1}^{\infty}\frac{A_n a_n}{2}e^{i(n\phi+\theta_n)}\left[e^{in\omega t} - e^{-t/\tau_p}\right] + u(t)\sum_{n=1}^{\infty}\frac{A_n a_n}{2}e^{-i(n\phi+\theta_n)}\left[e^{-in\omega t} - e^{-t/\tau_p}\right]\\
&= \underbrace{u(t)\sum_{n=1}^{\infty}A_n a_n\cos\left(n\left(\omega t+\phi\right)+\theta_n\right)}_{\text{Steady state}} + \underbrace{\left[y(0) - u(t)\sum_{n=1}^{\infty}A_n a_n\cos\left(n\phi+\theta_n\right)\right]e^{-t/\tau_p}}_{\text{Transient}}.
\end{aligned}
$$

Here $A_n e^{i\theta_n} \equiv \tau_p/\left(1+in\omega\tau_p\right)$ is the TF between transmitter voltage and coil current for the n-th harmonic of the fundamental frequency. Assuming that the previous pulse segment has reached steady-state, the condition for transient cancellation at $t = T$ is given by

$$
\sum_{n=1}^{\infty}A_n a_n\cos\left(n\left(\omega T+\phi\right)+\theta_n\right) = \sum_{n=1}^{\infty}A_n a_n\cos\left(n\left(\omega T+\phi'\right)+\theta_n\right). \qquad \text{(A.3)}
$$

This equation requires the two steady-state waveforms to cross each other at the switching instant $t = T$. In general it must be solved numerically. However, the situation is considerably simplified if $\theta_n \approx -\left(\pi/2\right)\ \forall n$ and the coil current contains only odd harmonics. Both requirements are usually satisfied in practice. The first only requires that $\omega\tau_p \gg 1$, while the second requires the coil current to have half-wave symmetry. In this case the waveform is anti-symmetric about zero within every cycle. More precisely, it satisfies the condition $y\left(t \pm T/2\right) = -y(t)$ where $T = 2\pi/\omega$ is the period of the fundamental component. For two-phase switching transmitters such as H-bridges and half-bridges, the half-wave symmetry condition is satisfied if identical switching waveforms are used for both phases within a single RF cycle. In such cases a symmetric square wave voltage waveform is applied across the coil, so the coil current becomes a triangle wave.

If both requirements are satisfied, the condition for eliminating transients at $t = T$ is given by

$$
\sum_{n=1}^{\infty}\frac{a_n}{n\omega}\cos\left(n\left(\omega T+\phi\right)-\frac{\pi}{2}\right) = \sum_{n=1}^{\infty}\frac{a_n}{n\omega}\cos\left(n\left(\omega T+\phi'\right)-\frac{\pi}{2}\right). \qquad \text{(A.4)}
$$

Here we have used the fact that $A_n \approx 1/(n\omega)\ \forall n$ if $\omega\tau_p \gg 1$. We also note that

$$\cos\left(n\left(\omega T \pm \pi + \phi\right) - \pi/2\right) = -\cos\left(n\left(\omega T + \phi\right) - \pi/2\right)$$

for any odd value of n, so there are still two solutions within each RF cycle that are separated by $\omega T = \pi$ (although there may be more). In addition, we see that

$$\cos\left(n\left(\omega T + \phi\right) - \frac{\pi}{2}\right) = \begin{cases} \cos\left(n\left(\omega T + \phi - \frac{\pi}{2}\right)\right),\ n = 1, 5, 9... \\ -\cos\left(n\left(\omega T + \phi - \frac{\pi}{2}\right)\right),\ n = 3, 7, 11... \end{cases} \tag{A.5}$$

We can therefore write the condition for transient cancellation as

$$\sum_{n=1}^{\infty} \frac{a_n(-1)^{(n-1)/2}}{n\omega} \cos\left(n\left(\omega T + \phi - \frac{\pi}{2}\right)\right) = \sum_{n=1}^{\infty} \frac{a_n(-1)^{(n-1)/2}}{n\omega} \cos\left(n\left(\omega T + \phi' - \frac{\pi}{2}\right)\right). \tag{A.6}$$

Since $\cos(x)$ is an even function, this equation will be satisfied for the n-th harmonic if the corresponding phases on both sides are inverses of each other, i.e., if $(\omega T + \phi - \pi/2) = -(\omega T + \phi' - \pi/2)$.

The latter condition is independent of the value of n. It is also identical to the condition derived earlier for the sinusoidal case (after substituting $\theta = \pi/2$). As a result, waveform intersections are unaffected by the presence of harmonics, and coil current transients can be cancelled by applying the same timing corrections as derived for the fundamental component. However, the amount of transmitter power saved by this procedure will depend on the shape of the input waveform.

Appendix B. Derivation of Coil Current in Tuned Probes

Appendix B.1. Derivation of the Differential Equation

Using Kirchoff's current law, the relevant circuit equations for the circuit shown in Fig. 5 are

$$V_c = L\frac{dI_c}{dt} + R_c I_c \tag{B.1}$$

and

$$C\frac{dV_c}{dt} + I_c = \frac{V_s(t) - V_c}{R_s}, \tag{B.2}$$

where V_c is the voltage across the coil, L is the inductance of the coil, R_c is the series resistance of the coil, I_c is the current through the coil, C is the sum of the capacitance of the tuning capacitor and the parallel parasitic capacitance of the coil, and V_s is the open-circuit voltage of the transmitter.

These first-order ODEs can be combined into a single second-order ODE given by

$$LC\frac{d^2I_c}{dt^2} + \left(R_cC + \frac{L}{R_s}\right)\frac{dI_c}{dt} + \left(1 + \frac{R_c}{R_s}\right)I_c = \frac{V_s(t)}{R_s}. \tag{B.3}$$

We define i) a dimensionless time variable $\tau \equiv \omega_r t$ where $\omega_r = 1/\sqrt{LC}$ is the probe resonance frequency, and ii) the characteristic impedance $Z_0 \equiv \sqrt{L/C}$. In terms of these variables, eqn. (B.3) is written as

$$\frac{d^2I_c}{d\tau^2} + \left(\frac{R_c}{Z_0} + \frac{Z_0}{R_s}\right)\frac{dI_c}{d\tau} + \left(1 + \frac{R_c}{R_s}\right)I_c = \frac{V_s(t)}{R_s}. \tag{B.4}$$

Eqn. (B.4) is mathematically identical to that of a driven, damped harmonic oscillator given by

$$\frac{d^2y}{d\tau^2} + 2\gamma\frac{dy}{d\tau} + \omega_n^2 y = f(\tau), \tag{B.5}$$

where the following identifications apply: $y \equiv I_c$, $\omega_n \equiv \sqrt{1 + \frac{R_c}{R_s}}$, $\gamma \equiv \frac{1}{2}\left(\frac{R_c}{Z_0} + \frac{Z_0}{R_s}\right)$, and $f(\tau) \equiv \frac{V_s(\tau)}{R_s}$.

Appendix B.2. Homogeneous Solution

The solution to eqn. (B.4) can be found by separately finding the homogeneous and inhomogeneous (non driven and driven respectively) solutions to the equation. We start by finding the general solution of eqn. (B.4) for the homogeneous case, which is obtained by setting $f(\tau) = 0$ on the right-hand side. Physically, this corresponds to the natural (not driven) dynamics of the system. The resulting

homogeneous ODE has a general solution of

$$y_h(\tau) = c_1 e^{\lambda_1 \tau} + c_2 e^{\lambda_2 \tau} \quad \text{and}$$
$$\dot{y}_h(\tau) = c_1 \lambda_1 e^{\lambda_1 \tau} + c_2 \lambda_2 e^{\lambda_2 \tau}, \tag{B.6}$$

where the coefficients c_1 and c_2 depend on the initial conditions of the system.

By substituting the solution in (B.6) back into the ODE, we find that the exponential rates λ_1 and λ_2 must satisfy the quadratic equation

$$\lambda^2 + (2\gamma)\,\lambda + \omega_n^2 = 0, \tag{B.7}$$

which has the solutions

$$\lambda_{1,2} = -\gamma \pm \sqrt{\gamma^2 - \omega_n^2} \equiv -\gamma \pm \alpha. \tag{B.8}$$

Given the initial conditions (i.e., the values of y and $dy/d\tau$ at $\tau = 0$), the coefficients c_1 and c_2 can be found by solving the following set of linear equations:

$$\begin{bmatrix} y_h(0) \\ \dot{y}_h(0) \end{bmatrix} = \begin{bmatrix} 1 & 1 \\ \lambda_1 & \lambda_2 \end{bmatrix} \begin{bmatrix} c_1 \\ c_2 \end{bmatrix}$$
$$\Rightarrow \begin{bmatrix} c_1 \\ c_2 \end{bmatrix} = \begin{bmatrix} 1 & 1 \\ \lambda_1 & \lambda_2 \end{bmatrix}^{-1} \begin{bmatrix} y_h(0) \\ \dot{y}_h(0) \end{bmatrix} = \tfrac{1}{(\lambda_2 - \lambda_1)} \begin{bmatrix} \lambda_2 & -1 \\ -\lambda_1 & 1 \end{bmatrix} \begin{bmatrix} y_h(0) \\ \dot{y}_h(0) \end{bmatrix} = \tfrac{1}{2\alpha} \begin{bmatrix} -\lambda_2 y_h(0) + \dot{y}_h(0) \\ \lambda_1 y_h(0) - \dot{y}_h(0) \end{bmatrix}. \tag{B.9}$$

Appendix B.3. Inhomogeneous (Driven) Solution

We now find a particular solution of the inhomogeneous (driven) ODE for a complex exponential RF input $f(\tau) = u(\tau)e^{i(\omega\tau+\phi)}$. The analytical solution is found to be

$$y_d(\tau) = u(\tau)\frac{e^{i\phi-(\gamma+\alpha)\tau}\left[(i\omega+\gamma)\left(1-e^{2\alpha\tau}\right)+\alpha\left(-1-e^{2\alpha\tau}+2e^{(i\omega+\gamma+\alpha)\tau}\right)\right]}{2\alpha\left[\left({\omega_n}^2-\omega^2\right)+2i\gamma\omega\right]}, \tag{B.10}$$

where $\alpha \equiv \sqrt{\gamma^2-\omega_n^2}$ as defined earlier. From eqn. (B.10), the derivative of y_d with respect to time is

$$\dot{y}_d(\tau) = \frac{ie^{i\phi-(\gamma+\alpha)\tau}\left[(i\omega_n^2-\gamma\omega)\left(1-e^{2\alpha\tau}\right)+\alpha\omega\left(-1-e^{2\alpha\tau}+2e^{(i\omega+\gamma+\alpha)\tau}\right)\right]}{2\alpha\left[\left({\omega_n}^2-\omega^2\right)+2i\gamma\omega\right]}, \quad \tau \geq 0. \tag{B.11}$$

As an example, the real and imaginary parts of y and $dy/d\tau$ corresponding to these expressions are shown in Fig. B.25 for the following set of parameters: $\phi = 0$, $\omega_n = 1$, $\omega = 1.1$, and $\gamma = \{0.1, 0.2, ...0.9\}$. Each solution starts from zero and then builds up to a steady-state over a few cycles. This build-up (or settling) period is of great interest for NMR applications, since it determines the maximum rate at which the RF pulse can be amplitude or phase modulated.

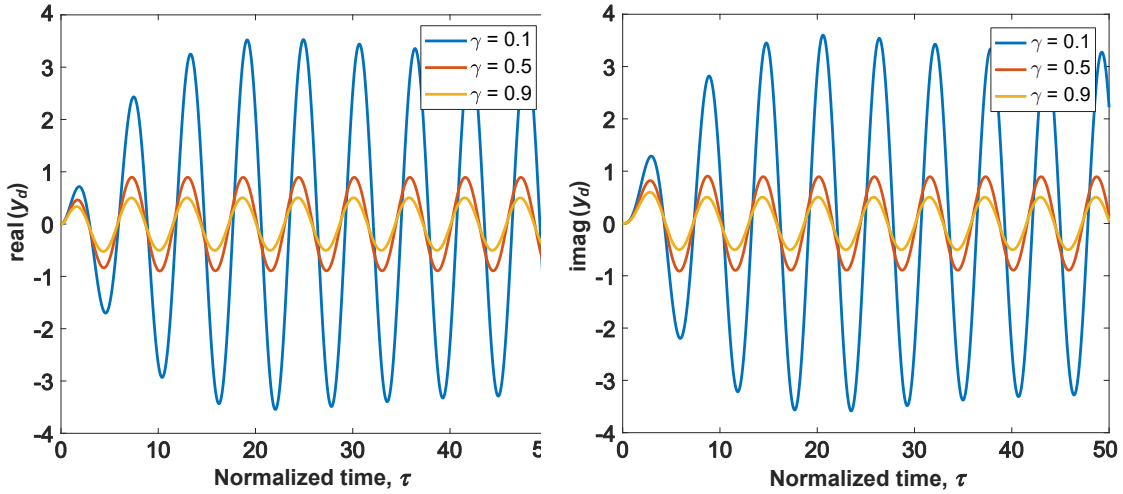

(a) (b)

Figure B.25: Simulated step response of the real coil current (a) and imaginary coil current (b) for various values of the damping parameter γ. We assumed the following set of parameters: $\phi = 0$, $\omega_n = 1$, $\omega = 1.1$, and $\gamma = 0.1$, 0.5, and 0.9.

The particular solution can be rewritten as the sum of asymptotic (steady-state) and transient terms:

$$y_d(\tau) = \frac{u(\tau)e^{i\phi}}{[({\omega_n}^2 - \omega^2) + 2i\gamma\omega]} \left[\underbrace{e^{i\omega\tau}}_{\text{Steady state}} + \underbrace{\frac{(\lambda_2 - i\omega)}{2\alpha} e^{\lambda_1\tau} - \frac{(\lambda_1 - i\omega)}{2\alpha} e^{\lambda_2\tau}}_{\text{Transient}} \right]$$
$$\dot{y}_d(\tau) = \frac{e^{i\phi}}{[({\omega_n}^2 - \omega^2) + 2i\gamma\omega]} \left[i\omega e^{i\omega\tau} + \frac{\lambda_1 (\lambda_2 - i\omega)}{2\alpha} e^{\lambda_1\tau} - \frac{\lambda_2 (\lambda_1 - i\omega)}{2\alpha} e^{\lambda_2\tau} \right], \quad \tau \geq 0. \tag{B.12}$$

For single-coil systems, the RF input is a sinusoid given by $f(\tau) = u(\tau)\cos(\omega\tau + \phi)$. Since this is the real part of the complex exponential RF input and the governing ODE is linear, the resulting particular solution is simply the real part of the complex solution shown in (eqn. B.12).

Defining the steady-state gain and phase shift as $A(\omega) = \left[(\omega_n^2 - \omega^2)^2 + (2\gamma\omega)^2\right]^{-1/2}$ and $\theta(\omega) = -\tan^{-1}\left(\frac{2\gamma\omega}{\omega_n^2 - \omega^2}\right)$, respectively, the particular solution for sinusoidal inputs can be written as

$$y_d(\tau) = A(\omega)u(\tau) \left[\underbrace{\cos(\omega\tau + \phi + \theta)}_{\text{Steady state}} + \underbrace{a_1 e^{\lambda_1\tau} + a_2 e^{\lambda_2\tau}}_{\text{Transient}} \right], \tag{B.13}$$

where

$$a_1 \equiv \frac{\lambda_2 \cos(\phi + \theta) + \omega \sin(\phi + \theta)}{2\alpha} \quad \text{and} \quad \mathrm{a}_2 \equiv -\frac{\lambda_1 \cos(\phi + \theta) + \omega \sin(\phi + \theta)}{2\alpha}. \tag{B.14}$$

Note that $\theta = -\pi/2$ when $\omega = \omega_n$. Also, the time derivative of the inhomogeneous solution is

$$\dot{y}_d(\tau) = A(\omega) \left[-\omega \sin(\omega\tau + \phi + \theta) + a_1\lambda_1 e^{\lambda_1\tau} + a_2\lambda_2 e^{\lambda_2\tau} \right], \quad \tau \geq 0. \tag{B.15}$$

Appendix B.4. General Solution

The general solution to eqn. (B.5) is the sum of the homogeneous solution (eqn. (B.6)) and inhomogeneous solution (eqn. (B.13)):

$$y(\tau) = y_h(\tau) + y_d(\tau) = A(\omega)u(\tau) \left[\underbrace{\cos(\omega\tau + \phi + \theta)}_{\text{Steady state}} + \underbrace{(a_1 + c_1) a_1 e^{\lambda_1\tau} + (a_2 + c_2) e^{\lambda_2\tau}}_{\text{Transient}} \right]. \tag{B.16}$$

The driven solution must have $y_d(0) = 0$ and $\dot{y}_d(0) = 0$, so $y(0) = y_h(0)$ and $\dot{y}(0) = \dot{y}_h(0)$. Thus,

$$\begin{bmatrix} c_1 \\ c_2 \end{bmatrix} = \begin{bmatrix} 1 & 1 \\ \lambda_1 & \lambda_2 \end{bmatrix}^{-1} \begin{bmatrix} y(0) \\ \dot{y}(0) \end{bmatrix} = \frac{1}{2\alpha} \begin{bmatrix} -\lambda_2 y(0) + \dot{y}(0) \\ \lambda_1 y(0) - \dot{y}(0) \end{bmatrix}. \tag{B.17}$$

Appendix B.5. Eliminating Switching Transients

Let us assume that the coil current has reached steady-state before the input phase changes from ϕ to ϕ' at time $\tau = T$. In this case the initial amplitudes of the transient components due to the homogeneous solution are c_1 and c_2. Thus,

$$\begin{aligned} y_d(T) &= A\cos(\omega T + \phi + \theta) \quad \text{and} \\ \dot{y}_d(T) &= -A\omega\sin(\omega T + \phi + \theta). \end{aligned} \tag{B.18}$$

Plugging eqn. (B.18) into eqn. (B.9), we get

$$\begin{bmatrix} c_1 \\ c_2 \end{bmatrix} = -\frac{A}{2\alpha} \begin{bmatrix} \lambda_2\cos(\omega T + \phi + \theta) + \omega\sin(\omega T + \phi + \theta) \\ -\lambda_1\cos(\omega T + \phi + \theta) - \omega\sin(\omega T + \phi + \theta) \end{bmatrix}, \tag{B.19}$$

where we have used the fact that $\lambda_1 - \lambda_2 = 2\alpha$ to simplify the expression. The initial amplitudes of the transient components due to the particular solution are

$$\begin{bmatrix} a_1 \\ a_2 \end{bmatrix} = \frac{A}{2\alpha} \begin{bmatrix} \lambda_2\cos(\omega T + \phi' + \theta) + \omega\sin(\omega T + \phi' + \theta) \\ -\lambda_1\cos(\omega T + \phi' + \theta) - \omega\sin(\omega T + \phi' + \theta) \end{bmatrix}. \tag{B.20}$$

In order to cancel out the transients, we need to have $\begin{bmatrix} a_1 \\ \\ a_2 \end{bmatrix} + \begin{bmatrix} c_1 \\ \\ c_2 \end{bmatrix} = 0$, which implies that:

$$\lambda_2 \cos(\omega T + \phi' + \theta) + \omega \sin(\omega T + \phi' + \theta) = \lambda_2 \cos(\omega T + \phi + \theta) + \omega \sin(\omega T + \phi + \theta),$$
$$\lambda_1 \cos(\omega T + \phi' + \theta) + \omega \sin(\omega T + \phi' + \theta) = \lambda_1 \cos(\omega T + \phi + \theta) + \omega \sin(\omega T + \phi + \theta). \quad \text{(B.21)}$$

These equations have no general solutions apart from the trivial case of no phase change ($\phi' = \phi$). Unlike in the case of the untuned coil, there is therefore no general way to cancel the transients produced by a phase-modulated RF pulse. However, these conditions are simplified in the over-coupled case, i.e., when $\gamma \gg 1$. In this case $\lambda_1 \approx 0$ and $\lambda_2 \approx -2\gamma$, resulting in

$$-2\gamma \cos(\omega T + \phi' + \theta) + \omega \sin(\omega T + \phi' + \theta) = -2\gamma \cos(\omega T + \phi + \theta) + \omega \sin(\omega T + \phi + \theta),$$
$$\omega \sin(\omega T + \phi' + \theta) = \omega \sin(\omega T + \phi + \theta). \quad \text{(B.22)}$$

The second condition can be ignored for operation around probe resonance ($\omega \approx 1$). In this case, $\gamma \gg \omega$ and the transient elimination condition reduces to $\cos(\omega T + \phi' + \theta) = \cos(\omega T + \phi + \theta)$, which is identical to that of an untuned coil. This result confirms that over-coupled tuned probes and untuned probes have similar dynamics in transmit mode.

Appendix C. Derivation of Coil Current in Matched Probes

Appendix C.1. Calculation of Coil Current

Given the circuit equations, some algebra results in a single equation that connects V_s to I_c:

$$\frac{sC_2V_s}{I_c} = s^3C_1C_2R_sL + s^2\left(L(C_1 + C_2) + C_1C_2R_sR_c\right) + s\left((C_1 + C_2)R_c + C_2R_s\right) + 1. \quad \text{(C.1)}$$

In order to simplify eqn. (C.1), we define a normalized (dimensionless) time variable $\tau = \omega_p t$, where

$\omega_p = \sqrt{LC_1}$. The corresponding normalized Laplace transform variable is $\sigma = s/\omega_p$, resulting in

$$\frac{\sigma C_2}{\sqrt{LC_1}}\frac{V_s}{I_c} = \sigma^3\frac{C_1C_2R_sL}{(LC_1)^{3/2}} + \sigma^2\frac{(L(C_1+C_2)+C_1C_2R_sR_c)}{LC_1} + \sigma\frac{((C_1+C_2)R_c+C_2R_s)}{\sqrt{LC_1}} + 1. \tag{C.2}$$

Next, we define the dimensionless variable $m = C_1/C_2$ (generally $m = 4-10$), which results in

$$\begin{aligned}\frac{\sigma C_1}{m\sqrt{LC_1}}\frac{V_s}{I_c} &= \sigma^3\frac{{C_1}^2R_sL}{m(LC_1)^{3/2}} + \sigma^2\frac{\left(LC_1(m+1)+{C_1}^2R_sR_c\right)}{mLC_1} + \sigma\frac{(C_1(m+1)R_c+C_1R_s)}{m\sqrt{LC_1}} + 1,\\ \frac{\sigma}{m}\sqrt{\frac{C_1}{L}}\frac{V_s}{I_c} &= \frac{\sigma^3}{m}\sqrt{\frac{C_1}{L}}R_s + \frac{\sigma^2}{m}\left((m+1)+\frac{C_1}{L}R_sR_c\right) + \frac{\sigma}{m}\sqrt{\frac{C_1}{L}}\left((m+1)R_c+R_s\right).\end{aligned} \tag{C.3}$$

Next, we define the characteristic impedance of the probe as $Z_0 = \sqrt{L/C_1}$; this variable has dimensions of Ohms. Eqn. (C.3) now simplifies to

$$\begin{aligned}\frac{\sigma}{mZ_0}\frac{V_s}{I_c} &= \frac{\sigma^3}{mZ_0}R_s + \frac{\sigma^2}{m}\left((m+1)+\frac{R_sR_c}{Z_0^2}\right) + \frac{\sigma}{mZ_0}\left((m+1)R_c+R_s\right),\\ \frac{\sigma}{R_s}\frac{V_s}{I_c} &= \sigma^3 + \sigma^2\left((m+1)\frac{Z_0}{R_s}+\frac{R_c}{Z_0}\right) + \sigma\left((m+1)\frac{R_c}{R_s}+1\right) + \frac{mZ_0}{R_s}.\end{aligned} \tag{C.4}$$

We can now directly write the corresponding differential equation in the normalized time domain by remembering that $\mathcal{L}\left(f'(t)\right) = sF(s) - f(0)$ where $\mathcal{L}(\cdot)$ denotes the Laplace transform. Thus, assuming zero initial conditions, we can simply make the transformation $\sigma \leftrightarrow d/d\tau$ to get

$$\begin{aligned}&\frac{d^3I_c}{d\tau^3} + c_3\frac{d^2I_c}{d\tau^2} + c_2\frac{dI_c}{d\tau} + c_1I_c = \frac{1}{R_s}\frac{dV_s}{dt}, \quad \text{where}\\ c_3 = \left((m+1)\frac{Z_0}{R_s}+\frac{R_c}{Z_0}\right), &\quad c_2 = \left((m+1)\frac{R_c}{R_s}+1\right), \quad \text{and} \quad c_1 = \frac{mZ_0}{R_s}.\end{aligned} \tag{C.5}$$

This is a simple third-order ODE with constant coefficients that can be solved using standard ODE solvers. For simplicity, the coil current I_c is further normalized to its ideal value I_{c_0} for a perfectly-matched probe in steady-state. The latter can be derived by using an energy conservation argument. For perfect matching, the input impedance of the probe is R_s, so the source current is $I_{s0} = V_{s0}/\left(R_s + Z_{in}\right) = V_{s0}/(2R_s)$ where V_{s_0} is the amplitude of the source voltage. Thus, the power delivered by the source is

$P_s = I_{s0}^2 R_s/2 = V_{s0}^2/(8R_s)$. The same power must be dissipated in the coil's series resistance R_c, so

$$P_s = \frac{V_{s_0}^2}{8R_s} = P_c = \frac{{I_{c_0}}^2 R_c}{2} \quad \Rightarrow \quad I_{c_0} = \frac{V_{s_0}}{2\sqrt{R_c R_s}}. \tag{C.6}$$

Appendix C.2. Calculation of the Receiver Transfer Function

We solve for the receiver TF from V_{in} to V_{out} by breaking the circuit into two voltage dividers. The first is from V_{in} to V_c and the other is from V_c to V_{out}. The first TF is solved in the s-domain to be

$$\frac{V_c}{V_{in}} = \frac{\left(\frac{1}{sC_1} || \left(R_s + \frac{1}{sC_1}\right)\right)}{sL + R_c + \left(\frac{1}{sC_1} || \left(R_s + \frac{1}{sC_1}\right)\right)} = \frac{\frac{m+sC_1R_s}{(m+1)+sC_1R_s}}{s^2LC_1 + sC_1R_c + \frac{m+sC_1R_s}{(m+1)+sC_1R_s}}. \tag{C.7}$$

We now use the results from eqn. (C.7) to solve for the TF between V_{out} and V_{in}. The resulting TF is

$$\frac{V_{out}}{V_{in}} = \frac{V_c}{V_{in}} \frac{R_s}{R_s + \frac{1}{sC_2}} = \frac{V_c}{V_{in}} \frac{sC_1R_s}{m + sC_1R_s}. \tag{C.8}$$

Plugging eqn. (C.7) into eqn. (C.8) and simplifying the expression, the resulting TF is

$$\frac{V_{out}}{V_{in}} = \frac{sC_1R_s}{[sC_1R_s + (m+1)]\,[s^2LC_1 + sC_1R_c] + sC_1R_s + m}. \tag{C.9}$$

The normalized Laplace transform variable is $\sigma = s/\omega_p = s\sqrt{LC_1}$, resulting in a normalized TF of

$$G_R(\sigma) = \frac{V_{out}}{V_{in}} = \frac{\sigma}{\sigma^3 + c_3\sigma^2 + c_2\sigma + c_1}, \tag{C.10}$$

where c_i ($i = \{1, 2, 3\}$) has the same definitions as in the transmitter model.

References

[1] Robert L. Kleinberg, A. Sezginer, D. D. Griffin, and M. Fukuhara. Novel NMR apparatus for investigating an external sample. *Journal of Magnetic Resonance (1969)*, 97(3):466–485, 1992.

[2] Martin D Hürlimann and Nicholas J Heaton. NMR well logging. In *Mobile NMR and MRI*, pages 11–85. Royal Society of Chemistry Cambridge, 2015.

[3] R. J. Schoelkopf and S. M. Girvin. Wiring up quantum systems. *Nature*, 451(7179):664, 2008.

[4] I. N. Hincks, C. E. Granade, Troy W. Borneman, and David G. Cory. Controlling quantum devices with nonlinear hardware. *Physical Review Applied*, 4(2):024012, 2015.

[5] Atsushi Kubo and Shinji Ichikawa. Ultra-broadband NMR probe: Numerical and experimental study of transmission line NMR probe. *Journal of Magnetic Resonance*, 162(2):284–299, 2003.

[6] D Murphree, SB Cahn, D Rahmlow, and D DeMille. An easily constructed, tuning free, ultra-broadband probe for NMR. *Journal of Magnetic Resonance*, 188(1):160–167, 2007.

[7] Timothy Hopper, Soumyajit Mandal, David Cory, Martin Hürlimann, and Yi-Qiao Song. Low-frequency NMR with a non-resonant circuit. *Journal of Magnetic Resonance*, 210(1):69–74, 2011.

[8] Soumyajit Mandal, Shin Utsuzawa, David G. Cory, Martin Hürlimann, Martin Poitzsch, and Yi-Qiao Song. An ultra-broadband low-frequency magnetic resonance system. *Journal of Magnetic Resonance*, 242:113–125, 2014.

[9] Raluca M Fratila, M Victoria Gomez, Stanislav Sỳkora, and Aldrik H Velders. Multinuclear nano-liter one-dimensional and two-dimensional NMR spectroscopy with a single non-resonant microcoil. *Nature communications*, 5(1):1–8, 2014.

[10] DI Hoult and Paul C Lauterbur. The sensitivity of the zeugmatographic experiment involving human samples. *Journal of Magnetic Resonance (1969)*, 34(2):425–433, 1979.

[11] N Bloembergen and RV Pound. Radiation damping in magnetic resonance experiments. *Physical Review*, 95(1):8, 1954.

[12] H. Michael Gach, Irving J. Lowe, David P. Madio, Arvind Caprihan, Stephen A. Altobelli, Dean O. Kuethe, and Eiichi Fukushima. A programmable pre-emphasis system. *Magnetic Resonance in Medicine*, 40(3):427–431, 1998.

[13] S. Johanna Vannesjo, Yolanda Duerst, Laetitia Vionnet, Benjamin E. Dietrich, Matteo Pavan, Simon Gross, Christoph Barmet, and Klaas P. Pruessmann. Gradient and shim pre-emphasis by inversion of a linear time-invariant system model. *Magnetic Resonance in Medicine*, 78(4):1607–1622, 2017.

[14] Kazuyuki Takeda, Yutaka Tabuchi, Makoto Negoro, and Masahiro Kitagawa. Active compensation of RF-pulse transients. *Journal of Magnetic Resonance*, 197(2):242–244, 2009.

[15] Y Tabuchi, M Negoro, K Takeda, and M Kitagawa. Total compensation of pulse transients inside a resonator. *Journal of Magnetic Resonance*, 204(2):327–332, 2010.

[16] Ulrich Haeberlen. *High Resolution NMR in solids selective averaging: supplement 1 advances in magnetic resonance*, volume 1. Elsevier, 2012.

[17] Leon Bosman, PK Madhu, Shimon Vega, and Elena Vinogradov. Improvement of homonuclear dipolar decoupling sequences in solid-state nuclear magnetic resonance utilising radiofrequency imperfections. *Journal of magnetic resonance*, 169(1):39–48, 2004.

[18] Thomas M. Barbara, Joel F. Martin, and Jon G. Wurl. Phase transients in NMR probe circuits. *Journal of Magnetic Resonance (1969)*, 93(3):497–508, 1991.

[19] M. Mehring and J. S. Waugh. Phase transients in pulsed NMR spectrometers. *Review of Scientific Instruments*, 43(4):649–653, 1972.

[20] H.J. Hogben, M. Krzystyniak, G.T.P. Charnock, P.J. Hore, and Ilya Kuprov. Spinach – a software library for simulation of spin dynamics in large spin systems. *Journal of Magnetic Resonance*, 208(2):179 – 194, 2011.

[21] Mikhail Veshtort and Robert G Griffin. SPINEVOLUTION: A powerful tool for the simulation of solid and liquid state NMR experiments. *Journal of Magnetic Resonance*, 178(2):248–282, 2006.

[22] Mads Bak, Jimmy T Rasmussen, and Niels Chr Nielsen. SIMPSON: A general simulation program for solid-state NMR spectroscopy. *Journal of Magnetic Resonance*, 213(2):366–400, 2011.

[23] Martin D. Hürlimann and Douglas D. Griffin. Spin dynamics of Carr–Purcell–Meiboom–Gill-like sequences in grossly inhomogeneous B_0 and B_1 fields and application to NMR well logging. *Journal of Magnetic Resonance*, 143(1):120 – 135, 2000.

[24] Sujatha Vathyam, Sanghyuk Lee, and Warren S Warren. Homogeneous NMR spectra in inhomogeneous fields. *Science*, 272(5258):92–96, 1996.

[25] Thomas E. Skinner, Timo O. Reiss, Burkhard Luy, Navin Khaneja, and Steffen J. Glaser. Application of optimal control theory to the design of broadband excitation pulses for high-resolution NMR. *Journal of Magnetic Resonance*, 163(1):8 – 15, 2003.

[26] Navin Khaneja, Timo Reiss, Cindie Kehlet, Thomas Schulte-Herbrüggen, and Steffen J Glaser. Optimal control of coupled spin dynamics: design of NMR pulse sequences by gradient ascent algorithms. *Journal of magnetic resonance*, 172(2):296–305, 2005.

[27] Van D.M. Koroleva, Soumyajit Mandal, Yi-Qiao Song, and Martin D. Hürlimann. Broadband CPMG sequence with short composite refocusing pulses. *Journal of Magnetic Resonance*, 230:64 – 75, 2013.

[28] Soumyajit Mandal, Van D.M. Koroleva, Troy W. Borneman, Yi-Qiao Song, and Martin D. Hürlimann. Axis-matching excitation pulses for CPMG-like sequences in inhomogeneous fields. *Journal of Magnetic Resonance*, 237:1 – 10, 2013.

[29] Soumyajit Mandal, Troy W. Borneman, Van D. M. Koroleva, and Martin D. Hürlimann. Direct optimization of signal-to-noise ratio of CPMG-like sequences in inhomogeneous fields. *Journal of Magnetic Resonance*, 247:54–66, 2014.

[30] Mattias Edén. Computer simulations in solid-state NMR. I. Spin dynamics theory. *Concepts in Magnetic Resonance Part A*, 17A(1):117–154, 1 2003.

[31] Zdeněk Tošner, Rasmus Andersen, Baltzar Stevensson, Mattias Edén, Niels Chr Nielsen, and

Thomas Vosegaard. Computer-intensive simulation of solid-state NMR experiments using SIMPSON. *Journal of Magnetic Resonance*, 246:79–93, 2014.

[32] Luke J Edwards, DV Savostyanov, ZT Welderufael, Donghan Lee, and Ilya Kuprov. Quantum mechanical NMR simulation algorithm for protein-size spin systems. *Journal of Magnetic Resonance*, 243:107–113, 2014.

[33] Ludmilla Guduff, Ahmed J Allami, Carine van Heijenoort, Jean-Nicolas Dumez, and Ilya Kuprov. Efficient simulation of ultrafast magnetic resonance experiments. *Physical Chemistry Chemical Physics*, 19(27):17577–17586, 2017.

[34] Dan Ma, Vikas Gulani, Nicole Seiberlich, Kecheng Liu, Jeffrey L Sunshine, Jeffrey L Duerk, and Mark A Griswold. Magnetic resonance fingerprinting. *Nature*, 495(7440):187–192, 2013.

[35] M Guéron. A coupled resonator model of the detection of nuclear magnetic resonance: Radiation damping, frequency pushing, spin noise, and the signal-to-noise ratio. *Magnetic resonance in medicine*, 19(1):31–41, 1991.

[36] Laurence W Nagel. *SPICE2: A computer program to simulate semiconductor circuits*. PhD thesis, University of California at Berkeley, 1975.

[37] David I Hoult and RE Richards. The signal-to-noise ratio of the nuclear magnetic resonance experiment. *Journal of Magnetic Resonance (1969)*, 24(1):71–85, 1976.

[38] Soumyajit Mandal, Sangwon Oh, and Martin D. Hürlimann. Absolute phase effects on CPMG-type pulse sequences. *Journal of Magnetic Resonance*, 261:121–132, 2015.

[39] F. Bloch and A. Siegert. Magnetic resonance for nonrotating fields. *Physical Review*, 57(6):522, 1940.

[40] Yuhua Cheng, Gaofeng Wang, and Maysam Ghovanloo. Analytical modeling and optimization of small solenoid coils for millimeter-sized biomedical implants. *IEEE Transactions on Microwave Theory and Techniques*, 65(3):1024–1035, 2016.

[41] George Turin. An introduction to matched filters. *IRE transactions on Information theory*, 6(3):311–329, 1960.

[42] Richard G Spencer. Equivalence of the time-domain matched filter and the spectral-domain matched filter in one-dimensional NMR spectroscopy. *Concepts in Magnetic Resonance Part A*, 36(5):255–265, 2010.

[43] Mason Greer, Cheng Chen, and Soumyajit Mandal. An easily reproducible, hand-held, single-sided, MRI sensor. *Journal of Magnetic Resonance*, 308:106591, 2019.

[44] Mathieu Sarracanie and Najat Salameh. Low-field MRI: how low can we go? A fresh view on an old debate. *Front Phys*, 8:172, 2020.